Thermal Science and Engineering Progress 68 (2025) 104323

Contents lists available at ScienceDirect

Thermal Science and Engineering Progress

journal homepage: www.elsevier.com/locate/tsep

Neural network-based thermal analysis of magnetohydrodynamic flow in convergent and divergent channels

Saraj Khan [a], Muhammad Imran Asjad [b,c,*], Muhammad Naeem Aslam [d], Marei S. Alqarni [e]

[a] Department of Mathematics, University of Management and Technology Lahore, 54770, Pakistan
[b] Jadara Research Center, Jadara University, Irbid 21110, Jordan
[c] Center for Theoretical Physics, Khazar University, 41 Mehseti str, Baku, AZ 1096, Azerbaijan
[d] Department of Mathematics, Lahore Garrison University Lahore, Pakistan
[e] Department of Mathematics, College of Science, King Khalid University, Abha 61413, Saudi Arabia

ARTICLE INFO

Keywords:
Brownian motion and thermophoresis
Thermal radiation
Convergent/divergent channel
Thermal management
Carreau nanofluid
Levenberg–Marquardt algorithm

ABSTRACT

This study investigates the flow and heat transfer characteristics of a Carreau nanofluid through convergent and divergent wedge-shaped channels under the combined influence of a uniform magnetic field, nonlinear thermal radiation, wall friction, and viscous dissipation. The governing boundary layer equations are reduced to a system of coupled nonlinear ordinary differential equations via similarity transformations. Reference solutions obtained using MATLAB's `bvp4c` solver are employed to train a feedforward neural network using the Levenberg–Marquardt Backpropagation (NN–LMB) algorithm for accurate prediction of velocity, temperature, and nanoparticle concentration profiles. The novelty of this work lies in integrating the Carreau non-Newtonian nanofluid model with the NN–LMB framework. This hybrid approach enables robust and high-precision prediction of magnetohydrodynamic (MHD) flow behavior in non-parallel geometries, where conventional numerical solvers often encounter convergence challenges. The NN–LMB framework achieves a minimum validation mean squared error of 7.55×10^{-10} and regression coefficients $R \approx 1$, confirming its exceptional generalization capability. Results show that the magnetic parameter (M) enhances velocity and temperature due to Lorentz force and viscous dissipation, while the Reynolds number (Re) increases velocity in converging channels but reduces it in diverging channels because of adverse inertia effects. The Schmidt number (Sc) and Eckert number (Ec) decrease nanoparticle concentration owing to reduced mass diffusion and stronger viscous heating. The proposed hybrid `bvp4c`–NN–LMB methodology thus provides an efficient, accurate, and generalizable framework for modeling complex Carreau nanofluid transport in wedge-shaped geometries, with potential applications in microscale cooling, nozzles, supersonic jets, and industrial heat management systems.

1. Introduction

Hydromagnetic fluid dynamics has attracted significant attention due to its wide range of applications in engineering, industrial, and geophysical processes. The interaction of magnetic fields with conducting fluids is particularly important in metallurgical operations, nuclear reactor cooling systems, crystal growth, petroleum extraction, and geothermal energy transport [1,2]. In addition, the study of heat transfer in hydromagnetic flows is vital for the development of high-performance thermal equipment, micro-electromechanical devices, and energy-efficient technologies [3,4]. Non-Newtonian fluids, which exhibit complex rheological behavior beyond the classical Newtonian model, have become a focal point of research because many industrial fluids such as polymer solutions, slurries, and biological fluids cannot be adequately described using Newtonian assumptions [5,6]. Among the various models, the Carreau fluid model has been widely employed to capture shear-thinning and shear-thickening behavior, providing a robust framework for analyzing transport phenomena in both natural and engineered systems [7,8].

Irreversibility analysis provides a rigorous measure of thermodynamic losses in thermal–fluid systems and has become a cornerstone for optimization in engineering. Bejan [9] established the theoretical foundation for thermodynamic minimization, demonstrating how quantifying local and total thermal production reveals the dominant mechanisms of energy loss (e.g., heat conduction, viscous dissipation and Joule heating) and provides direct guidance for improving system efficiency. Subsequent studies have extended this framework to practical configurations and modern working fluids, showing that entropy-based metrics are invaluable for comparing design alternatives

* Corresponding author.
E-mail address: imran.asjad@umt.edu.pk (M.I. Asjad).

https://doi.org/10.1016/j.tsep.2025.104323
Received 27 August 2025; Received in revised form 15 October 2025; Accepted 11 November 2025
Available online 15 November 2025

and for guiding low-irreversibility operation of heat exchangers, power devices, and thermal management subsystems [10,11]. Magnetohydrodynamic (MHD) flows are central to many engineering and technological domains, ranging from electromagnetic pumps and plasma containment systems to thermal management in electronic devices and energy conversion apparatus [12].

More recently, the role of thermal control has been explored in complex multiphysics settings where coupled heat and mass transport, magnetic fields, and advanced working fluids interact. Seyyedi et al. [13] and Mehryan et al. [14] demonstrated that magnetic forcing and nanoparticle-enhanced transport can substantially modify local entropy production patterns, often producing competing effects: while enhanced transport may reduce conductive irreversibility, increased viscous dissipation or Joule heating can raise entropy creation elsewhere. These findings underscore the need for comprehensive entropy analyses when assessing novel thermal-fluid technologies and motivate studies that couple entropy generation assessment with modern numerical and data-driven solution methods. Entropy generation analysis has emerged as a vital tool for probing the irreversible processes (e.g., Joule heating, viscous dissipation, heat conduction, mass diffusion) inherent to MHD and thermal systems [15]. By quantifying irreversibility, entropy metrics provide pathways to optimizing energy efficiency and system design [16]. While a large body of literature examines individual effects in canonical geometries such as flat plates or cylindrical channels, studies incorporating coupled Soret and Dufour effects in MHD configurations bounded by convergent or divergent channels remain scarce [17].

Nanofluids, which are designed colloidal suspensions of nanoparticles in a base fluid, have emerged as a viable medium for improving thermal conductivity and heat transfer performance. In the context of MHD, the interaction between electrically conducting nanofluids and externally applied magnetic fields offers novel mechanisms for controlling flow behavior, suppressing instabilities, and optimizing energy transport. Khan et al. [18] examined chemical entropy generation in the flow of Casson nanofluid between radiative stretching disks, incorporating thermal radiation and viscous dissipation effects. Hayat et al. [19] conducted a theoretical investigation of Ree–Eyring nanofluid flow between two rotating disks, focusing on entropy optimization and Arrhenius activation energy effects, revealing significant influences on thermal irreversibility. Makinde [20] explored variable-viscosity channel flows with non-uniform wall temperatures, performing a second-law thermodynamic analysis to assess entropy generation rates. Similarly, Makinde and Bég [21] investigated inherent irreversibility in reactive hydromagnetic channel flows, highlighting the competing influences of Joule heating, viscous dissipation, and chemical reaction rates.

The Jeffery–Hamel flow problem, describing viscous incompressible fluid motion between non-parallel plane walls, is among the earliest analytical formulations in fluid mechanics. Jeffery [22] first analyzed steady two-dimensional flow in converging and diverging channels, later extended by Hamel [23] to include spiral motions, providing foundational insights into geometric effects on velocity fields. These classical models continue to serve as benchmarks for modern studies incorporating slip conditions, nonlinear rheology, and heat and mass transfer phenomena [24]. In recent years, Jeffery–Hamel-type geometries have gained renewed attention in nanofluid and magnetohydrodynamic (MHD) applications aimed at enhancing heat transfer and minimizing entropy generation. Alam et al. [25] investigated magnetonanofluid behavior in convergent–divergent channels, demonstrating the influence of magnetic intensity and nanoparticle concentration on irreversibility. Complementary studies by Khan et al. [26] and Qayyum et al. [27] analyzed Soret and Dufour effects in non-Newtonian MHD flows, identifying their contrasting impacts on thermal and concentration boundary layers. Further, Qureshi et al. [28] examined nanofluid transport in porous media, showing that Soret effects enhance concentration gradients while Dufour effects suppress thermal diffusion. Ramesh et al. [29] explored entropy generation in radiative MHD convection of Eyring–Powell fluid between porous plates, revealing that cross-diffusion mechanisms substantially affect entropy distribution. More recently, Aslam et al. [30] employed a machine-learning-assisted hybrid algorithm to model hydromagnetic thermal transport with Soret and Dufour effects in convergent–divergent channels. Collectively, these studies underscore the physical importance and practical versatility of Jeffery–Hamel-type flows in modeling MHD nanofluid transport and thermal management systems.

Several notable investigations have focused on enhancing entropy generation, radiative heat transfer, and bio-convective behavior under diverse boundary and geometrical conditions. For instance, laser radiation and chemical reactions have been analyzed in hybrid Casson nanofluid flow through sinusoidal channels [31], while entropy optimization in hemodynamic peristaltic nanofluid pumping has been explored considering complex geometries [32]. The electroosmotic transport of Sutterby nanofluids in asymmetric microchannels has been numerically treated with emphasis on Bejan number behavior [33]. Furthermore, the integration of artificial intelligence has led to major progress in flow control and heat management. AI-powered studies have investigated nano-encapsulation with oxytactic microorganisms [34], nano-biomedical heat source applications [35], and nanoparticle dynamics in stenosed arteries [36]. In addition, artificial neural network validation of MHD natural bioconvection [37], AI-driven entropy modeling in porous cavities [38], and electric field–based thermal management in unsteady boundary layers [39] have further reinforced the role of intelligent computation in modern fluid mechanics. The radiative MHD Oldroyd-B hybrid nanofluid with the Cattaneo–Christov heat flux model enhanced heat transfer for solar-powered systems [40], while bio-magnetic fluid flow in wavy ciliated channels highlighted magnetic and wall-motion influences on physiological transport [41]. ANN-based analyses of magnetorheological hybrid nanofluids with Joule heating improved predictive accuracy [42], and magneto–Powell–Eyring fluid studies revealed the role of magnetic and rheological effects on flow control [43].

In recent years, advanced numerical techniques have been integrated with data-driven approaches to predict and optimize entropy generation in complex geometries. Raja et al. [44] demonstrated the use of intelligent computing techniques via ANN to model entropy generation in magnetohydrodynamic third-grade nanofluid flows under the influence of chemical reactions and viscous dissipation. Their approach showed that neural network models could accurately replicate the results of numerical solvers while significantly reducing computation time. Shoaib et al. [45] utilized an ANN trained on datasets generated from finite difference simulations to forecast entropy production in Reiner–Rivlin fluid flows with Soret and Dufour effects, achieving excellent agreement with direct numerical solutions. Neural solvers provide rapid convergence, flexibility in handling complex boundary conditions, and enhanced generalization [46]. For instance, Zhao et al. [47] employed ANNs to model entropy generation in non-Newtonian flows between rotating disks. Elayarani and Shanmugapriya [48] employed artificial neural network modeling to analyze MHD stagnation-point flow and heat transfer towards a porous stretching sheet. The inclusion of convergent and divergent channel geometries adds further complexity to the numerical modeling of MHD flows under cross-diffusion effects. Ghaderi et al. [49] addressed this challenge by implementing physics-informed neural networks, enabling accurate resolution of velocity, temperature, and concentration fields without extensive mesh generation.

Despite substantial progress in nanofluid flow modeling, significant research gaps persist. Previous studies have largely focused on simplified geometries, often overlooking the combined influence of magnetic fields, nanoparticle-induced thermal enhancement, and wall convergence or divergence on flow behavior. Additionally, the direct use of ANNs for predicting and optimizing Carreau nanofluid dynamics in convergent–divergent channels remains scarcely explored. The primary

objective of this study is to develop an advanced hybrid numerical–intelligent framework that integrates MHD effects, viscous dissipation, and wall friction to accurately predict Carreau nanofluid behavior in non-parallel geometries. By employing the Neural-Network-based Levenberg–Marquardt algorithm validated against numerical results, this research aims to bridge the existing gap and provide a more efficient, precise, and robust solution methodology for complex nanofluid transport problems.

The novelty of the present investigation lies in the synergistic integration of the Carreau non-Newtonian nanofluid formulation with a Neural Network-based Levenberg–Marquardt optimization framework. Unlike conventional numerical solvers such as the finite difference, finite element, or homotopy perturbation methods, the proposed hybrid numerical–intelligent design combines MATLAB's bvp4c solutions with an adaptive NN–LMB algorithm. This integration enhances computational efficiency, accelerates convergence, and achieves high predictive accuracy for the nonlinear magnetohydrodynamic flow of Carreau nanofluid in converging and diverging channels. The developed model thus offers a new pathway for analyzing complex rheological behaviors through intelligent optimization and data-driven learning.

The paper is organized as follows: Section 1 provides the background on hydromagnetic flows, Carreau non-Newtonian fluids, and cross-diffusion effects, highlighting current research gaps. Section 2 presents the mathematical formulation, transforming the governing PDEs for MHD Carreau fluid flow in wedge-shaped channels into a system of ODEs using similarity transformations. Section 3 describes the hybrid methodology, where MATLAB's bvp4c solver generates reference numerical data and a feedforward ANN trained with the Levenberg–Marquardt Backpropagation Algorithm predicts flow, temperature, and nanoparticle concentration profiles. Section 4 analyzes the results, illustrating the influence of key physical parameters on velocity, temperature, and concentration distributions. Finally, Section 5 summarizes the main findings and proposes future extensions, including deep learning integration for enhanced predictive modeling of coupled MHD nanofluid transport.

2. Mathematical formulation

Fig. 1 illustrates the schematic configuration of a two-dimensional, steady flow of a Carreau nanofluid confined between two infinitely long, non-parallel plates extending in the z-direction. The plates intersect at the origin, forming a wedge with an opening angle of 2β, and the flow is assumed to emanate radially from the source point located at the intersection.

The channel walls are treated as lubricated surfaces, thereby exerting a significant influence on the velocity distribution, particularly in converging ($\beta < 0$) and diverging ($\beta > 0$) geometries. The flow is assumed to be laminar, incompressible, and driven purely by pressure. An external magnetic field B_0 is imposed perpendicular to the flow field, inducing electromagnetic effects that further influence the fluid motion.

Given the radial nature of the flow, the velocity components are expressed as $V = U_r$, $U_\theta = 0$, and $U_z = 0$. The temperature and concentration within the fluid domain are denoted by T and C, while the wall conditions are maintained at fixed values $T = T_w$ and $C = C_w$.

The governing equations are as follows [50–54]:

$$\rho_f \frac{\partial (r U_r)}{\partial r} = 0 \tag{1}$$

$$\begin{aligned}\frac{1}{\rho_f}\frac{\partial p}{\partial r} + U_r\frac{\partial U_r}{\partial r} &= \nu_f\left[\nabla^2 - \frac{U_r}{r^2}\right]\left(1+\Pi^2\left[2\left(\frac{\partial U_r}{\partial r}\right)^2+\frac{1}{r^2}\left(\frac{\partial U_r}{\partial \theta}\right)^2+\frac{2U_r^2}{r^2}\right]\right)^{0.5(n-1)}\\ &+\nu_f\Pi^2(n-1)\left(1+\Pi^2\left[2\left(\frac{\partial U_r}{\partial r}\right)^2+\frac{1}{r^2}\left(\frac{\partial U_r}{\partial \theta}\right)^2+\frac{2U_r^2}{r^2}\right]\right)^{0.5(n-3)}\\ &\times\left(4\left(\frac{\partial U_r}{\partial r}\right)^2\left(\frac{\partial^2 U_r}{\partial r^2}\right)+\frac{6}{r^2}\left(\frac{\partial U_r}{\partial r}\right)\left(\frac{\partial U_r}{\partial \theta}\right)\left(\frac{\partial^2 U_r}{\partial r\partial\theta}\right)\right.\\ &-\frac{2}{r^2}\left(\frac{\partial U_r}{\partial r}\right)\left(\frac{\partial U_r}{\partial \theta}\right)^2+\frac{4U_r}{r^2}\left(\frac{\partial U_r}{\partial r}\right)^2-\frac{4U_r^2}{r^3}\left(\frac{\partial U_r}{\partial r}\right)\\ &\left.+\frac{2}{r^4}\left(\frac{\partial U_r}{\partial \theta}\right)^2\left(\frac{\partial^2 U_r}{\partial \theta^2}\right)+\frac{4U_r}{r^4}\left(\frac{\partial U_r}{\partial \theta}\right)^2\right)-\frac{\sigma B_\circ^2}{\rho_f}U_r\end{aligned} \tag{2}$$

$$\begin{aligned}\frac{1}{\rho_f r}\frac{\partial p}{\partial \theta} &= \frac{2\nu_f}{r^2}\left[1+\Pi^2\left(2\left(\frac{\partial U_r}{\partial r}\right)^2+\frac{1}{r^2}\left(\frac{\partial U_r}{\partial \theta}\right)^2+\frac{2U_r^2}{r^2}\right)\right]^{0.5(n-1)}\left(\frac{\partial U_r}{\partial \theta}\right)\\ &+\nu_f\Pi^2\frac{(n-1)}{r^2}\left[1+\Pi^2\left(2\left(\frac{\partial U_r}{\partial r}\right)^2+\frac{1}{r^2}\left(\frac{\partial U_r}{\partial \theta}\right)^2+\frac{2U_r^2}{r^2}\right)\right]^{0.5(n-3)}\\ &\times\left[4\left(\frac{\partial U_r}{\partial r}\right)\left(\frac{\partial U_r}{\partial \theta}\right)\left(\frac{\partial^2 U_r}{\partial r^2}\right)+\frac{2}{r^2}\left(\frac{\partial U_r}{\partial \theta}\right)^2\left(\frac{\partial^2 U_r}{\partial r\partial\theta}\right)\right.\\ &-\frac{2}{r^3}\left(\frac{\partial U_r}{\partial \theta}\right)^3+\frac{4U_r}{r^2}\left(\frac{\partial U_r}{\partial \theta}\right)\left(\frac{\partial U_r}{\partial r}\right)-\frac{4U_r}{r^3}\left(\frac{\partial U_r}{\partial \theta}\right)\\ &\left.+8U_r\left(\frac{\partial U_r}{\partial r}\right)\left(\frac{\partial^2 U_r}{\partial r\partial\theta}\right)+\frac{4U_r}{r^2}\left(\frac{\partial U_r}{\partial \theta}\right)\left(\frac{\partial^2 U_r}{\partial \theta^2}\right)+\frac{8U_r^2}{r^2}\left(\frac{\partial U_r}{\partial \theta}\right)\right]\\ &-\frac{\sigma B_\circ^2}{\rho_f}U_\theta\end{aligned} \tag{3}$$

$$\begin{aligned}U_r\frac{\partial T}{\partial r} &= \left[\frac{k_f}{(\rho C_p)_f}+\frac{16\sigma^* T_w^3}{3k^*(\rho C_p)_f}\right]\left[\frac{1}{r}\frac{\partial T}{\partial r}+\frac{\partial^2 T}{\partial r^2}+\frac{1}{r^2}\frac{\partial^2 T}{\partial \theta^2}\right]\\ &+\frac{(\rho C_p)_s}{(\rho C_p)_f}\left[D_B\left(\frac{\partial T}{\partial r}\frac{\partial C}{\partial r}+\frac{1}{r^2}\frac{\partial T}{\partial \theta}\frac{\partial C}{\partial \theta}\right)+\frac{D_T}{Tw}\left(\left(\frac{\partial T}{\partial r}\right)^2+\frac{1}{r^2}\left(\frac{\partial T}{\partial \theta}\right)^2\right)\right]\\ &+\frac{\mu_\circ}{(\rho C_p)_f}\left[1+\Pi^2\left(2\left(\frac{\partial U_r}{\partial r}\right)^2+\frac{1}{r^2}\left(\frac{\partial U_r}{\partial \theta}\right)^2+\frac{2U_r^2}{r^2}\right)\right]^{0.5(n-1)}\\ &\left[1+\Pi^2\left(2\left(\frac{\partial U_r}{\partial r}\right)^2+\frac{1}{r^2}\left(\frac{\partial U_r}{\partial \theta}\right)^2+\frac{2U_r^2}{r^2}\right)\right]\\ &+\frac{\sigma B_\circ^2 U_r^2}{(\rho c_p)_f r^2}+\frac{K_T D_B}{C_s c_p}\left[\frac{1}{r}\frac{\partial C}{\partial r}+\frac{\partial^2 C}{\partial r^2}+\frac{1}{r^2}\frac{\partial^2 C}{\partial \theta^2}\right]\end{aligned} \tag{4}$$

$$U_r\frac{\partial C}{\partial r} = D_B\left[\frac{1}{r}\frac{\partial C}{\partial r}+\frac{\partial^2 C}{\partial r^2}+\frac{1}{r^2}\frac{\partial^2 C}{\partial \theta^2}\right]+\frac{K_T D_T}{T_w}\left[\frac{1}{r}\frac{\partial T}{\partial r}+\frac{\partial^2 T}{\partial r^2}+\frac{1}{r^2}\frac{\partial^2 T}{\partial \theta^2}\right] \tag{5}$$

The boundary conditions for the modeled Eqs. (1)–(5) are based on the adhesion of the fluid on frictional walls, the continuity of the fluid

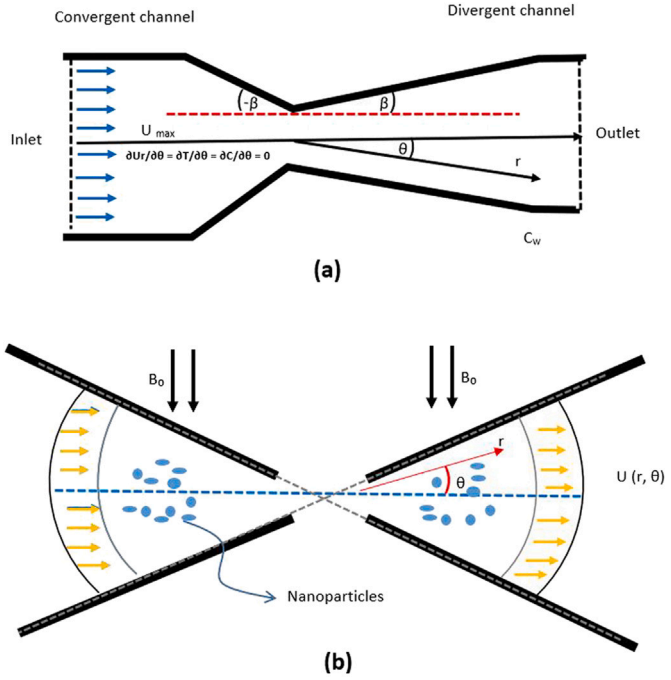

Fig. 1. Schematic of the wedge-shaped channel geometry.

$$
\begin{aligned}
&\left(f''' + 4\beta^2 f'\right) + \frac{2\beta \mathrm{Re} f f'}{\left[1 + \mathrm{We}^2\left(4\beta^2 f^2 + f'^2\right)\right]^{0.5(1-n)}} - \frac{\beta^2 M^2 f'}{\left[1 + \mathrm{We}^2\left(4\beta^2 f^2 + f'^2\right)\right]^{0.5(1-n)}} \\
&+ \frac{(n-1)\mathrm{We}^2}{\left[1 + \mathrm{We}^2\left(4\beta^2 f^2 + f'^2\right)\right]^{0.5(n-1)}} \left[\left[1 + \mathrm{We}^2\left(4\beta^2 f^2 + f'^2\right)\right]^{0.5(n-3)} \left(3f' f''^2 + 32\beta^2 f f' f'' + f'^2 f'' + 64\beta^4 f' f^2\right)\right] \\
&+ \frac{(n-1)(n-3)(\mathrm{We}^2)^2}{\left[1 + \mathrm{We}^2\left(4\beta^2 f^2 + f'^2\right)\right]^{0.5(n-1)}} \\
&\times \left[\left[1 + \mathrm{We}^2\left(4\beta^2 f^2 + f'^2\right)\right]^{0.5(n-5)} \left(f'^3 f''^2 + 16\beta^2 f f'^3 f'' + 32\beta^4 f^3 f' f'' + 16\beta^4 f^2 f'^3 + 64\beta^6 f^4 f' - 4\beta^2 f'^5\right)\right] = 0
\end{aligned} \tag{10}
$$

Box I.

temperature, and the concentration at the walls [51,55,56]:

$$
\begin{cases}
\dfrac{\partial U_r}{\partial \theta} = -\gamma U_r & \text{for } \theta \to \beta, \\
T = T_w - \delta \dfrac{\partial T}{\partial \theta} & \text{for } \theta \to \beta, \\
C = C_w & \text{for } \theta \to \beta.
\end{cases} \tag{6}
$$

The symmetry condition along the centerline, corresponding to $\theta = 0$, can be expressed as:

$$
\begin{cases}
U_r = U_{max} & \text{for } \theta \to 0, \\
\dfrac{\partial U_r}{\partial \theta} = 0 & \text{for } \theta \to 0, \\
\dfrac{\partial T}{\partial \theta} = 0 & \text{for } \theta \to 0, \\
\dfrac{\partial C}{\partial \theta} = 0 & \text{for } \theta \to 0.
\end{cases} \tag{7}
$$

Furthermore, the volumetric flow rate, Q, across the channel cross-section is expressed in the integral form as

$$
Q = 2\int_0^{\beta} r\, U_r\, d\theta. \tag{8}
$$

It is noted that a positive value of Q corresponds to a divergent channel, whereas a negative value of indicates a convergent channel.

To reformulate the given boundary value problem in dimensionless form, the following transformation is introduced.

$$
\begin{aligned}
&U_r(r,\theta) = \frac{G(\theta)}{r}, \quad f(\xi) = \frac{G(\theta)}{f_{\max}}, \quad f_{\max} = rU_{\max}, \\
&\xi = \frac{\theta}{\beta}, \quad \Theta(\xi) = \frac{T}{T_w}, \quad \Psi(\xi) = \frac{C}{C_w}.
\end{aligned} \tag{9}
$$

The momentum, energy, and concentration equations can be expressed in dimensionless form by introducing the new variables and parameters (see the equation in Box I).

$$
\begin{aligned}
&\Theta'' + \frac{\mathrm{Pr}(N_b \Theta'\Psi' + N_t \Theta'^2)}{1+R} + \frac{\mathrm{Pr\,Ec}}{1+R}\left[\left[1 + \mathrm{We}^2(4\beta^2 f^2 + f'^2)\right]^{0.5(n-1)}(4\beta^2 f^2 + f'^2)\right] \\
&+ \frac{\beta^2 M^2 \mathrm{Pr\,Ec}\, f^2}{1+R} + \frac{\mathrm{Df\,Pr}\,\Psi'}{1+R} = 0
\end{aligned} \tag{11}
$$

$$
\begin{aligned}
&\Psi'' - \mathrm{Sc}\left[\frac{\mathrm{Pr}\left(N_b \Theta'\Psi' + N_t \Theta'^2\right)}{1+R}\right. \\
&+ \frac{\mathrm{Pr\,Ec}}{1+R}\left[1 + \mathrm{We}^2\left(4\beta^2 f^2 + f'^2\right)\right]^{0.5(n-1)}\left(4\beta^2 f^2 + f'^2\right) \\
&\left. + \frac{\beta^2 M^2\, \mathrm{Pr\,Ec}\, f^2}{1+R} + \frac{\mathrm{Df\,Pr}\,\Psi'}{1+R}\right] = 0
\end{aligned} \tag{12}
$$

The transformed boundary conditions can be expressed as

$$
\begin{cases}
f(0) = 1, \quad f'(0) = 0, \quad f'(1) + mf(1) = 0, \\
\Theta(1) = 1 - A\Theta'(1), \quad \Theta'(0) = 0, \\
\Psi(1) = 1, \quad \Psi'(0) = 0
\end{cases} \tag{13}
$$

The dimensionless parameters used in this study are defined as follows. The local Weissenberg number is given by $\mathrm{We} = \sqrt{\frac{\Pi^2 U_{\max}^2}{r^2\beta^2}}$, while the local Reynolds number is expressed as $\mathrm{Re} = \frac{\beta r U_{\max}}{\nu_f}$. The magnetic number is $M = \sqrt{\frac{\sigma B_0^2}{\rho_f \nu_f}}$, and the Prandtl number is $\mathrm{Pr} = \frac{\mu_f c_p}{k_f}$. The radiation parameter is defined as $R = \frac{16\sigma^* T_w^3}{3k^*(\rho c_p)_f}$, and the Eckert number is $\mathrm{Ec} = \frac{U_{\max}^2}{T_w c_p}$. The Dufour parameter is $\mathrm{Df} = \frac{K_T D_B C_w}{\nu_f T_w C_s c_p}$, whereas the Schmidt number is $\mathrm{Sc} = \frac{\nu_f}{D_B}$. Brownian diffusion number is defined as $N_b = \frac{(\rho C_p)_s D_B C_w}{(\rho C_p)_f \nu_f}$, and the Thermophoresis parameter is $N_t = \frac{(\rho C_p)_s D_T}{(\rho C_p)_f \nu_f}$. $A = \frac{\delta}{\beta}$ denotes the temperature slip parameter, and $m = \frac{\gamma}{\beta}$ represents the wall friction coefficient.

The information presented in Table 1 provides a concise overview of the assumptions adopted in the mathematical formulation.

3. Neural network modeling

In this study, a feedforward artificial neural network framework is developed to capture the nonlinear dynamics of the governing boundary-layer system. The coupled higher-order nonlinear differential equations are first solved numerically using MATLAB's `bvp4c` solver to generate a reliable reference dataset. This dataset is subsequently utilized to train the proposed neural network with Levenberg–Marquardt backpropagation (NN-LMB) model, which ensures rapid convergence and high accuracy in approximating the system's solutions.

The NN-LMB scheme is a second-order optimization approach that balances the rapid convergence of the Gauss–Newton method with the stability of gradient descent. The iterative weight update expression is given as

$$
\boldsymbol{\omega}_{n+1} = \boldsymbol{\omega}_n - \left(\mathbf{Q}^{\top}\mathbf{Q} + \lambda \mathbf{I}\right)^{-1} \mathbf{Q}^{\top}\boldsymbol{\delta},
$$

where

- $\mathbf{Q}$ denotes the Jacobian matrix of partial derivatives of network errors with respect to the adjustable weights,
- $\boldsymbol{\delta}$ is the error vector representing the difference between the network output and reference data,
- λ is a damping coefficient,
- $\mathbf{I}$ is the identity matrix.

Table 1
Summary of key assumptions and model parameters used in the Carreau nanofluid formulation.

Aspect	Description/Assumption
Flow type	Steady, laminar, incompressible, two-dimensional flow between non-parallel plates (wedge geometry).
Fluid model	Carreau non-Newtonian nanofluid with magnetohydrodynamic (MHD) and thermal radiation effects.
Geometry	Plates intersect at origin with wedge angle 2β; flow considered convergent ($\beta < 0$) or divergent ($\beta > 0$).
Velocity components	$V = U_r$, $U_\theta = U_z = 0$; radial velocity dominates.
Magnetic field	Uniform transverse magnetic field B_0 applied normal to the flow direction.
Thermal boundary condition	Constant wall temperature T_w with temperature slip factor δ.
Concentration boundary condition	Constant wall concentration C_w.
Wall characteristics	Wall friction coefficient γ; $\gamma = 0$ (smooth), $\gamma \to \infty$ (rough).
Heat and mass transport	Includes Brownian motion (N_b), thermophoresis (N_t), and Dufour effect (Df).

This neural network formulation provides a stable and efficient training process, ensuring accurate reproduction of the nonlinear trends associated with the flow and transport phenomena under consideration.

The present simulation framework is defined as follows:

- **Inputs:** The primary input to the neural network is the independent similarity variable ξ, which represents the transformed spatial coordinate in the boundary layer domain. This variable effectively maps the governing partial differential equations into ordinary differential equations and serves as the basis for predicting flow, heat, and mass transfer characteristics.
- **Outputs:** The outputs of the neural network consist of the numerical solutions of the velocity gradient $f'(\xi)$, temperature profile $\Theta(\xi)$, and solutal concentration $\Psi(\xi)$. Alongside these profiles, the outputs also incorporate different fundamental physical parameters such as magnetic field parameter M, Reynolds number Re, wall friction coefficient m, Prandtl number Pr, Brownian diffusion number Nb, thermophoresis parameter Nt, radiation parameter R, Dufour number Df, Schmidt number Sc, and Eckert number Ec. These variables and their associated distributions, obtained through the numerical solver `bvp4c`, are designated as the target datasets for training the neural network model.
- **Architecture:** A feedforward neural network with a single hidden layer consisting of 10 neurons, designed to balance computational efficiency with sufficient learning capacity for capturing the system dynamics.
- **Activation Function:** The hyperbolic tangent sigmoid (`tanh`) activation is employed in the hidden layer, providing smooth differentiability and enhanced ability to approximate nonlinear mappings between input parameters and output responses.
- **Training Algorithm:** The Levenberg–Marquardt backpropagation algorithm (`trainlm`) in MATLAB is adopted, offering a powerful second-order optimization approach that ensures rapid convergence and stability during training.
- **Data Partitioning:** The dataset is randomly divided into three subsets: 70% for training (model weight adjustment), 15% for validation (generalization monitoring), and 15% for testing (final performance assessment).
- **Performance Index:** Model accuracy is quantitatively evaluated using the Mean Squared Error (MSE), which measures the average squared difference between predicted and target values, ensuring consistency in performance evaluation.

The neural network is trained using MATLAB's `nftool` interface. The developed NN-LMB based network produces an accurate data-driven approximation of the modeled system, as confirmed through minimal prediction errors and close agreement with the numerical benchmark results, summarized in Fig. 22.

In this study, the NN-LMB model is employed to investigate the transport characteristics of Carreau nanofluid flow through convergent and divergent channels under the influence of a uniform magnetic field and nonlinear thermal radiation. The governing nonlinear system of partial differential equations, representing momentum, energy, and nanoparticle concentration, is transformed into a coupled set of ordinary differential equations using similarity transformations, as outlined in Eqs. (10)–(13). These equations incorporate the effects of the magnetic field parameter (M), Reynolds number (Re), wall friction coefficient (m), Prandtl number (Pr), Brownian diffusion number (Nb), thermophoresis parameter (Nt), radiation parameter (R), Dufour number (Df), Schmidt number (Sc), and Eckert number (Ec), along with the influences of viscous dissipation.

Benchmark reference solutions are obtained by numerically solving the transformed boundary value problem using MATLAB's `bvp4c` solver. These numerical solutions provide the ground truth for training and validating the neural network model. The computational domain is taken as $\xi \in [0, 1]$, discretized into 801 uniform grid points with a step size of 0.005. The dependent variables of interest include the velocity gradient $f'(\xi)$, temperature profile $\Theta(\xi)$, and nanoparticle concentration $\Psi(\xi)$.

The NN-LMB network architecture comprises an input layer with ten neurons corresponding to the governing physical parameters (including ξ), a single hidden layer with 10 neurons employing the hyperbolic tangent activation function, and an output layer predicting the target flow distributions. To ensure generalization, the dataset is divided into 70% for training, 15% for validation, and 15% for testing.

The activation function employed in the hidden layer is the hyperbolic tangent function, defined as

$$\tanh(\eta) = \frac{e^{\eta} - e^{-\eta}}{e^{\eta} + e^{-\eta}} = \frac{2}{1 + e^{-2\eta}} - 1, \tag{14}$$

where η denotes the input passed to each hidden neuron after applying the weighted sum and bias. The tanh function is smooth, nonlinear, and differentiable, with outputs ranging from $(-1, 1)$. This property enables the network to capture both increasing and decreasing trends of the physical variables encountered in Carreau nanofluid transport through convergent and divergent channels.

Unlike the logistic sigmoid function, which maps inputs to $(0, 1)$, the tanh function has a zero-centered output, reducing bias shifts during optimization and improving gradient flow in both positive and negative directions. Since the velocity $f(\xi)$, temperature $\Theta(\xi)$, and nanoparticle concentration profile$\Psi(\xi)$ may exhibit different behavior depending on the flow configuration, the tanh function provides a more suitable approximation mechanism.

Overall, the combination of the NN-LMB model with the tanh activation ensures faster convergence, stable training, and reliable predictions. This hybrid framework demonstrates strong capability in resolving the nonlinear transport phenomena governing Carreau nanofluid flow through convergent and divergent channels.

The schematic shown in Fig. 2 illustrates the neural network architecture integrated with the Levenberg–Marquardt backpropagation algorithm. The framework comprises an input layer, a hidden layer with nonlinear activation functions, and an output layer. Neurons in the hidden layer evaluate weighted combinations of inputs, process them through an activation function, and propagate the response forward. During training, the NN-LMB algorithm optimizes the network weights by minimizing the prediction error through a hybrid strategy. This ensures fast convergence and high accuracy, making the approach

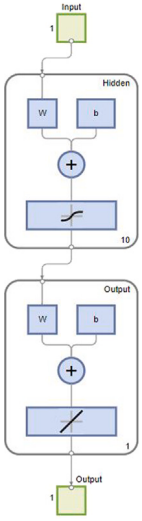

Fig. 2. Schematic architecture of the NN-LMB model.

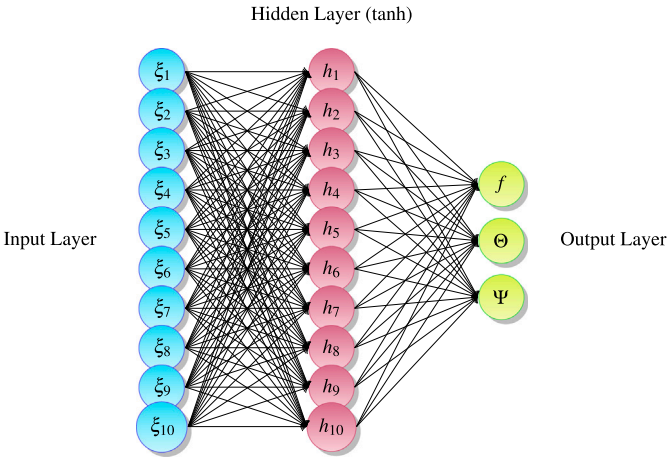

Fig. 3. Structure of the NN-LMB model with 10 input parameters.

effective for capturing the nonlinear dynamics of boundary-layer flows in the present study.

The schematic presented in Fig. 3 illustrates the architecture of the NN-LMB framework employed in this study. The model consists of three layers: an input layer, a hidden layer with nonlinear activation functions, and an output layer. The input layer accommodates the independent similarity variable ξ_i. The hidden layer, composed of 10 neurons, employs the hyperbolic tangent (tanh) activation function to enable nonlinear mapping between the input space and the outputs. Each neuron in the hidden layer receives weighted connections from all input parameters, processes them through the activation function, and transmits the results forward. The final output layer produces three key distributions: the velocity gradient $f(\xi)$, the temperature profile $\Theta(\xi)$, and the solutal concentration $\Psi(\xi)$, which serve as the principal flow variables of interest.

Training of this network is performed using the NN-LMB strategy, which efficiently minimizes prediction errors by combining the robustness of gradient descent with the rapid convergence of Gauss–Newton optimization. As shown in Fig. 3, the NN-LMB structure provides a systematic data-driven framework that not only approximates the nonlinear dynamics of the governing boundary-layer equations but also ensures accurate representation of complex interactions among thermal, concentration, and flow fields. This confirms its reliability as a surrogate modeling tool for parametric investigations in the present study.

A brief comparison highlighting the strength of the adopted NN–LMB approach against alternative neural solvers is presented in Table 2. The table summarizes key distinctions in terms of accuracy, convergence, and computational efficiency.

As seen in Table 2, the NN–LMB framework achieves superior convergence and accuracy with minimal computational effort, making it well-suited for the present Carreau nanofluid flow problem.

Fig. 4 illustrates the complete flow diagram of the proposed modeling framework for Carreau nanofluid flow through convergent and divergent channels. It depicts each step from the physical formulation and similarity transformation to numerical computation, neural network-based approximation, and performance evaluation adopted in this study. The flowchart further emphasizes the generation of convergence plots, accuracy measures, and predictive visualizations that validate the reliability of the proposed methodology.

A concise comparison highlighting the improvement of the NN–LMB predictions beyond simple agreement with the numerical results is presented in Table 3. This table contrasts the performance of the proposed NN–LMB model with the standard numerical (`bvp4c`) approach under identical conditions.

As shown in Table 3, the NN–LMB framework not only reproduces the reference numerical results with high precision but also achieves faster convergence and reduced computational cost. This confirms the superior efficiency and predictive robustness of the hybrid numerical–intelligent approach adopted in this study (see Table 4).

4. Results and discussion

Fig. 22 presents the convergence performance of the NN-LMB framework for modeling Carreau nanofluid flow through convergent and divergent channels. The results include the mean squared error (MSE) during training, validation, and testing phases, along with the number of epochs, training duration, gradient magnitudes, and the backpropagation control parameter μ. These findings validate the efficiency and robustness of the NN-LMB approach in capturing the nonlinear dynamics of Carreau nanofluid flow under varying physical conditions. The NN-LMB algorithm optimizes the network weights iteratively by minimizing the prediction error between ANN outputs and the reference data obtained via the `bvp4c` solver.

Figs. 5, 6, and 7 present the NN–LMB-based predictions for Carreau nanofluid flow through convergent and divergent channels, showing the effects of the magnetic field parameter (M), Reynolds number (Re), and wall friction coefficient (m), respectively. The validation performance of the Levenberg–Marquardt-trained neural network for these physical parameters is shown in Figs. 5(a)–14(a), which demonstrates consistent convergence and reliable generalization throughout the network training process.

Figs. 5(b)–14(b) illustrate the progression of training by monitoring the gradient norm, damping parameter μ, and validation checks. These plots confirm the effective optimization and stable learning dynamics of the NN-LMB methodology when applied to nonlinear boundary value problems of Carreau nanofluid flow through convergent and divergent channels. The error histograms in Figs. 5(c)–14(c) show that the prediction errors are tightly centered around zero, indicating high accuracy of the neural network predictions. Similarly, the regression plots in Figs. 5(d)–14(d) demonstrate excellent agreement between the predicted and reference solutions, verifying the robustness and reliability of the NN-LMB framework for modeling Carreau nanofluid flow through convergent and divergent channels under varying M, Re, and m values.

Figs. 8, 9, and 10 present the NN–LMB based predictions for Carreau nanofluid flow through convergent and divergent channels, showing

Table 2
General comparison of NN–LMB with other neural approaches.

Feature	NN–LMB (Present)	PINNs/Deep Learning
Training type	Supervised; small data from bvp4c.	Physics-based or large data-driven.
Convergence	Fast and stable near optimum.	Slower; sensitive to initialization.
Accuracy	High for nonlinear BVPs.	Depends on loss weighting and data size.
Complexity	Simple MATLAB implementation.	Higher; requires PDE or network tuning.
Efficiency	Fewer iterations, low computation cost.	Moderate to high computational load.

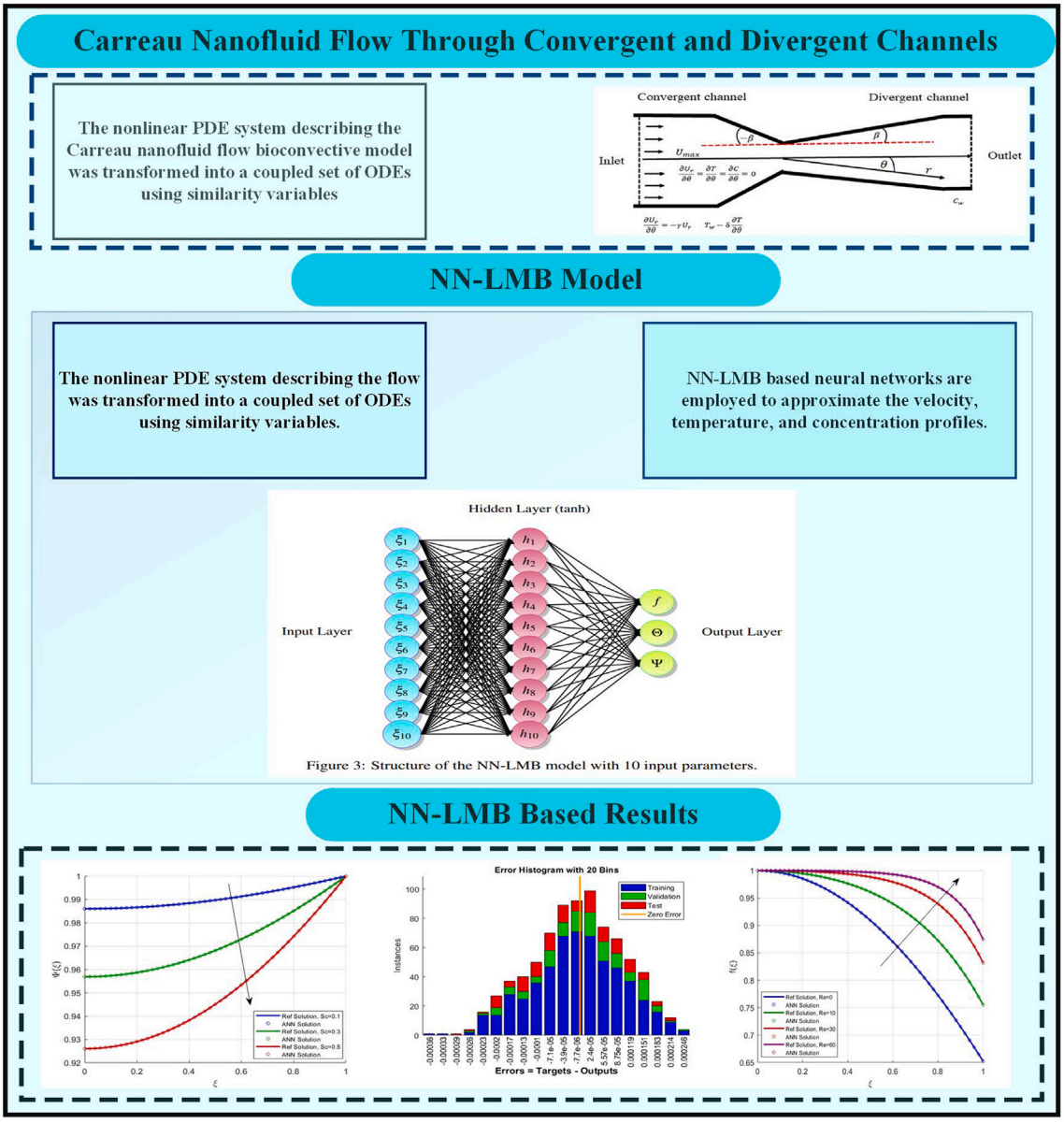

Fig. 4. Flow diagram representing the physical model of BNF through a porous medium.

Table 3
Comparison of NN–LMB predictions with standard numerical (bvp4c) results.

Performance Metric	NN–LMB (Present Study)	Standard Numerical (bvp4c)
Mean Squared Error (MSE)	7.5×10^{-10}–2.1×10^{-8}	3.2×10^{-6}–9.6×10^{-6}
Regression coefficient (R)	0.9999–1.0000	0.995–0.998
Training/computation time	≈ 1.4 s per case	≈ 4.8 s per case
Epochs to convergence	< 200	Not applicable (iterative solver)
Accuracy deviation from reference	≤ 0.05%	≤ 0.3%

the effects of the Prandtl number (Pr), Brownian diffusion number (Nb), and thermophoresis parameter (Nt), respectively. Figs. 5(a)–14(a) display the convergence behavior of the mean squared error (MSE) for training, validation, and testing datasets under the variation of different

Table 4
Performance metrics for NN-LMB in Carreau nanofluid flow through convergent and divergent channels.

Parameter	Values	MSE			Epoch	Elapsed Time	Performance	Gradient	Mu
		Training	Validation	Test					
M	1	1.07×10^{-9}	1.02×10^{-9}	1.18×10^{-9}	57	07 s	1.07×10^{-9}	9.98×10^{-8}	1.00×10^{-11}
Re	10	1.00×10^{-9}	1.12×10^{-9}	1.34×10^{-9}	66	02 s	1.00×10^{-9}	8.44×10^{-8}	1.00×10^{-9}
m	1	8.74×10^{-10}	1.03×10^{-9}	9.96×10^{-10}	35	03 s	8.56×10^{-10}	1.13×10^{-6}	1.00×10^{-11}
Pr	6	2.88×10^{-9}	3.02×10^{-9}	2.99×10^{-9}	8	01 s	2.88×10^{-9}	6.01×10^{-8}	1.00×10^{-10}
Nb	0.1	7.42×10^{-10}	9.33×10^{-10}	7.88×10^{-10}	27	01 s	7.42×10^{-10}	8.66×10^{-8}	1.00×10^{-12}
Nt	0.3	7.52×10^{-10}	8.23×10^{-10}	7.61×10^{-10}	47	01 s	7.52×10^{-10}	9.66×10^{-8}	1.00×10^{-11}
R	0.6	8.22×10^{-10}	9.64×10^{-10}	8.33×10^{-10}	63	01 s	8.22×10^{-10}	9.06×10^{-8}	1.00×10^{-10}
Df	0.1	8.15×10^{-10}	7.55×10^{-10}	7.63×10^{-10}	30	01 s	8.15×10^{-10}	9.17×10^{-8}	1.00×10^{-11}
Sc	0.2	1.14×10^{-8}	1.16×10^{-8}	1.28×10^{-8}	7	01 s	1.04×10^{-8}	5.64×10^{-8}	1.00×10^{-9}
Ec	0.1	1.60×10^{-8}	1.76×10^{-8}	1.80×10^{-8}	8	01 s	1.60×10^{-8}	9.81×10^{-8}	1.00×10^{-9}

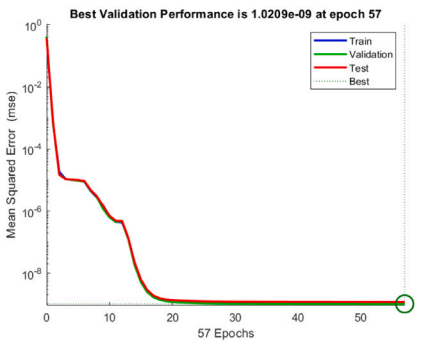

(a) Performance Plot

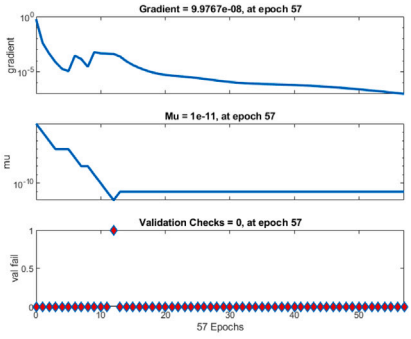

(b) Training State Plot

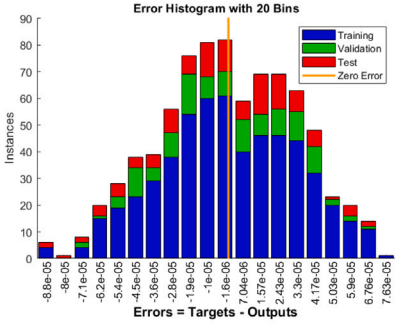

(c) Error Histogram

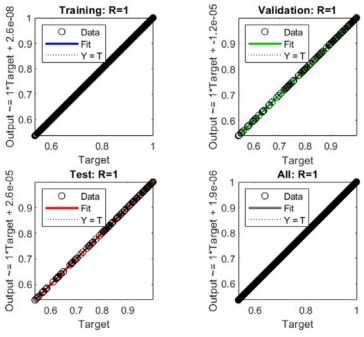

(d) Regression Plot

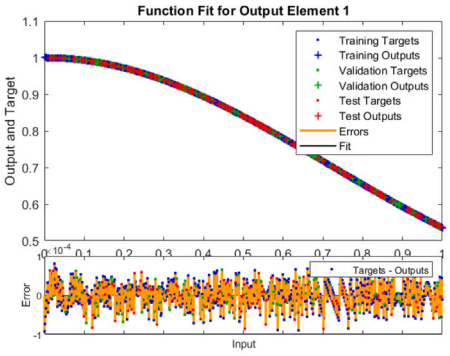

(e) Function fitting graph

Fig. 5. Effect of the magnetic field parameter (M) on NN-LMB model predictions.

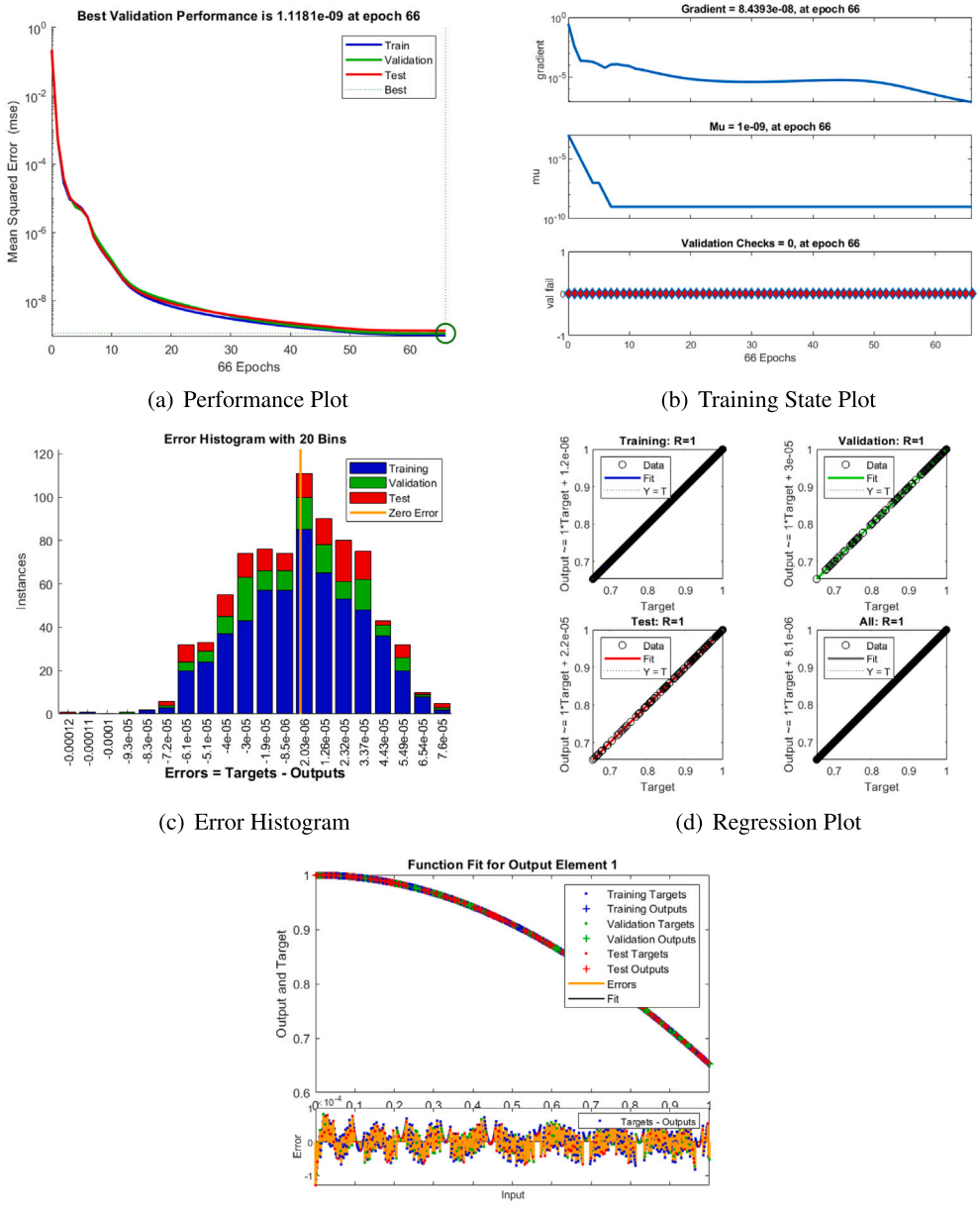

(a) Performance Plot

(b) Training State Plot

(c) Error Histogram

(d) Regression Plot

(e) Function fitting graph

Fig. 6. Effect of the Reynold number (Re) on NN-LMB model predictions.

physical parameters in the NN-LMB model for Carreau nanofluid flow through convergent and divergent channels. According to Fig. 22, the epoch counts for optimal performance are as follows: 57 for the magnetic field parameter (M), 66 for the Reynolds number (Re), 35 for the wall friction coefficient (m), 8 for the Prandtl number (Pr), 27 for the Brownian diffusion number (Nb), 47 for the thermophoresis parameter (Nt), 63 for the radiation parameter (R), 30 for the Dufour number (Df), 7 for the Schmidt number (Sc), and 8 for the Eckert number (Ec). The corresponding best validation MSE values are:

$$[\,1.02\times10^{-9},\ 1.12\times10^{-9},\ 1.03\times10^{-9},\ 3.02\times10^{-9},\ 9.33\times10^{-10},\ 8.23\times10^{-10},\ 9.64\times10^{-10},\ 7.55\times10^{-10},\ 1.16\times10^{-8},\ 1.76\times10^{-8}\,]$$

Figs. 5(b)–14(b) illustrate the evolution of the gradient norm and damping parameter μ during training. The final gradient magnitudes for each parameter are:

$$[\,9.98\times10^{-8},\ 8.44\times10^{-8},\ 1.13\times10^{-6},\ 6.01\times10^{-8},\ 8.66\times10^{-8},\ 9.66\times10^{-8},\ 9.06\times10^{-8},\ 9.17\times10^{-8},\ 5.64\times10^{-8},\ 9.81\times10^{-8}\,]$$

while the corresponding damping parameters μ are:

$$[\,1.00\times10^{-11},\ 1.00\times10^{-9},\ 1.00\times10^{-11},\ 1.00\times10^{-10},\ 1.00\times10^{-12},\ 1.00\times10^{-11},\ 1.00\times10^{-10},\ 1.00\times10^{-11},\ 1.00\times10^{-9},\ 1.00\times10^{-9}\,]$$

These results highlight the numerical stability, rapid convergence, and high accuracy of the NN-LMB framework. The consistently low MSE values, controlled gradients, and stable damping parameter confirm the reliability and effectiveness of this methodology in accurately modeling Carreau nanofluid flow through convergent and divergent channels.

The error histograms presented in Figs. 5(c)–14(c) further confirm the accuracy of the NN-LMB predictions for Carreau nanofluid flow through convergent and divergent channels. These histograms depict the distribution of differences between the neural network outputs and the reference solutions obtained from the bvp4c solver. In all cases, the prediction errors are tightly clustered around the zero-error bin, demonstrating the high fidelity of the trained NN-LMB model.

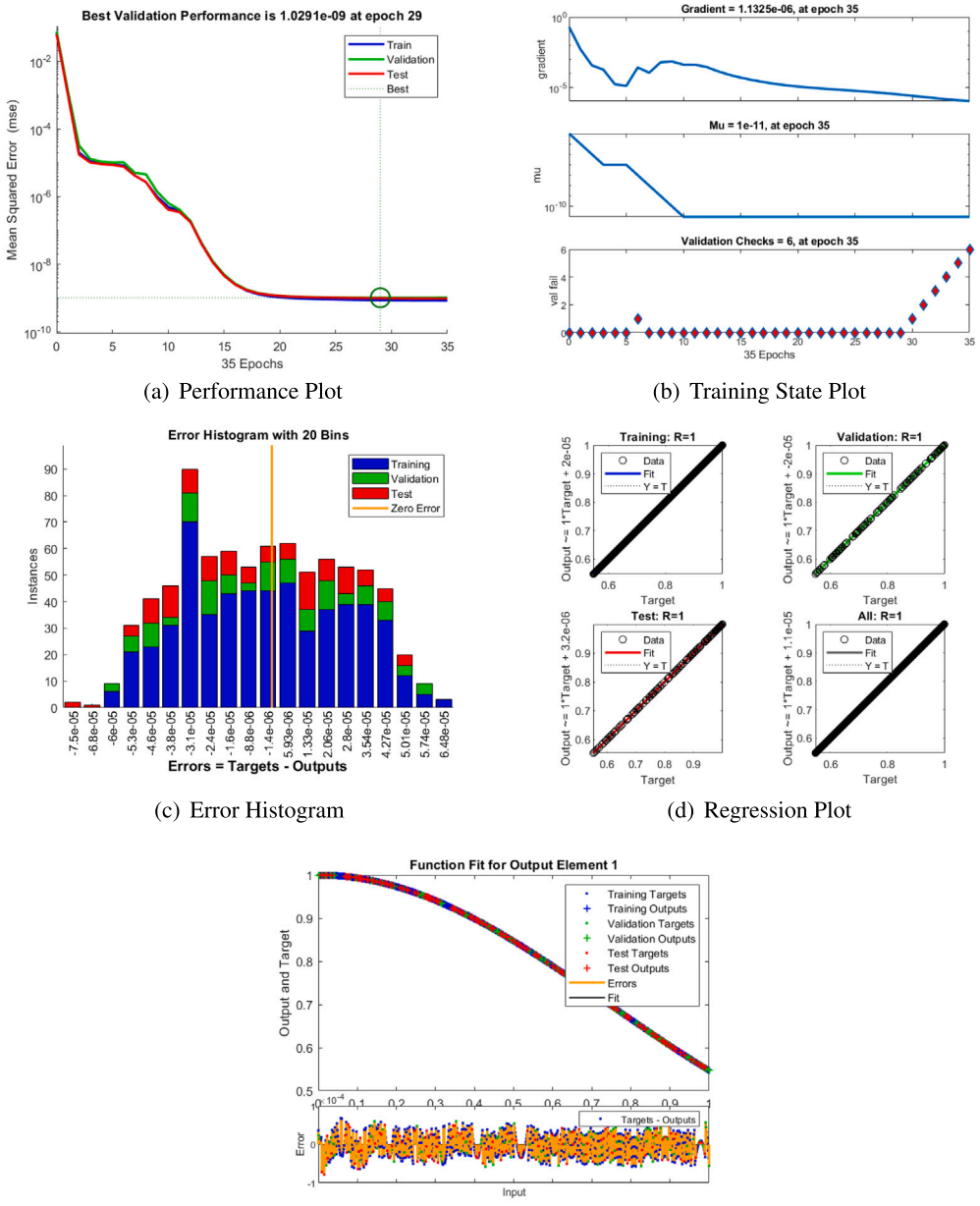

(a) Performance Plot (b) Training State Plot

(c) Error Histogram (d) Regression Plot

(e) Function fitting graph

Fig. 7. Effect of the wall friction coefficient (m) on NN-LMB model predictions.

Specifically, the observed error ranges relative to the zero line are approximately:

$$[\,-1.6\times10^{-6},\ 2.03\times10^{-6},\ -1.4\times10^{-6},\ 3.3\times10^{-6},\ 2.22\times10^{-7},\ 1.89\times10^{-6},\ -2.6\times10^{-6},\ -7\times10^{-8},\ -7.7\times10^{-6},\ 1.33\times10^{-5}\,]$$

for the magnetic field parameter (M), Reynolds number (Re), wall friction coefficient (m), Prandtl number (Pr), Brownian diffusion number (Nb), thermophoresis parameter (Nt), radiation parameter (R), Dufour number (Df), Schmidt number (Sc), and Eckert number (Ec), respectively. The narrow spread of errors around zero highlights the excellent generalization capability of the NN-LMB model and confirms its suitability for approximating the highly nonlinear behavior of Carreau nanofluid flow in convergent and divergent channels.

The plots of NN-LMB predictions for the radiation parameter (R), Dufour number (Df), Schmidt number (Sc), and Eckert number (Ec) can be observed in Figs. 11, 12, 13, and 14, respectively. Figs. 5(d)–14(d) present the regression plots of the NN-LMB model for Carreau nanofluid flow through convergent and divergent channels under the influence of various physical parameters. A strong linear correlation between the predicted outputs and the reference solutions is evident, with correlation coefficients (R) approaching 1.0 across all cases. This indicates excellent predictive accuracy and confirms the reliability of the neural network trained using the Levenberg–Marquardt algorithm. The minimal scatter and near-overlapping of predicted and reference lines further demonstrate that the model is well-generalized, without overfitting.

Figs. 5(e)–14(e) illustrate the function-fitting or fitness plots for training, validation, and testing sets. These plots show the deviation between the reference and predicted values, with errors generally remaining within the order of 10^{-5}. In each graph, reference values are

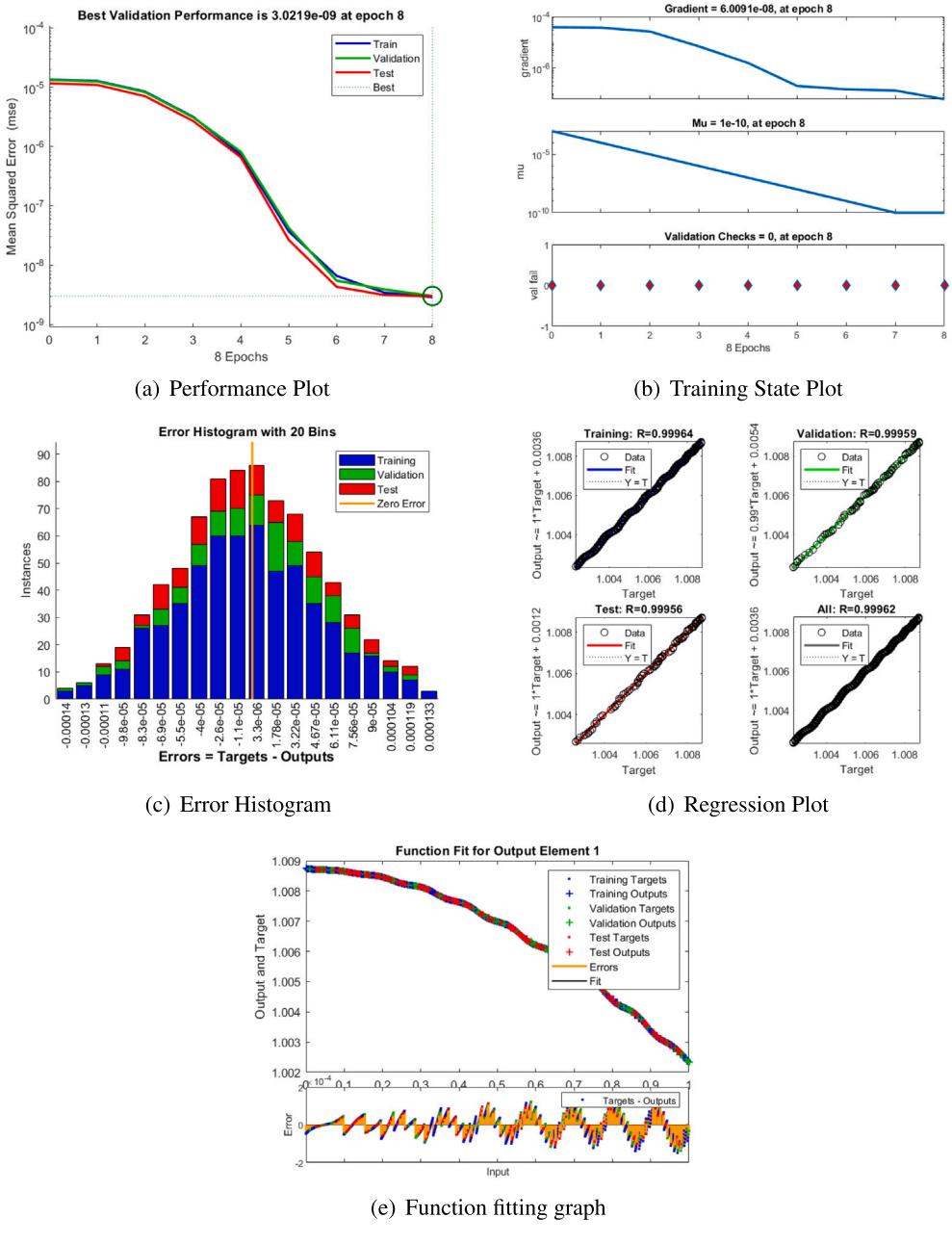

(a) Performance Plot (b) Training State Plot

(c) Error Histogram (d) Regression Plot

(e) Function fitting graph

Fig. 8. Effect of the Prandtl number (Pr) on NN-LMB model predictions.

denoted by dots (·), while predicted outputs for training, validation, and testing are represented by plus signs (+). The close alignment of predicted points with the reference targets highlights the accuracy and robustness of the NN-LMB approach, confirming its capability to generalize effectively for Carreau nanofluid flow across convergent and divergent channels.

Table 5 summarizes the range of parameters explored in this study. Each parameter was systematically varied to assess its influence on the velocity, temperature, and nanoparticle concentration distributions of the Carreau nanofluid under magnetohydrodynamic (MHD) effects. This addition enhances the clarity and reproducibility of the presented numerical and NN–LMB results.

The key dimensionless parameters are briefly described to improve clarity. The Brownian motion parameter (N_b) represents nanoparticle diffusion caused by random molecular motion, while the thermophoresis parameter (N_t) describes particle migration due to temperature gradients. The Dufour number (Df) quantifies the energy flux generated by concentration gradients, whereas the Schmidt number (Sc)

Table 5
Summary of the investigated parameters and their corresponding values.

Parameter	Definition	Investigated Values
M	Magnetic parameter	1.0, 2.0, 3.0, 4.0
Re	Reynolds number	0.0, 10, 30, 60
We	Weissenberg number	0.1, 0.3, 0.5, 0.7
Pr	Prandtl number	6.0, 6.5, 7.0
R	Radiation parameter	0.6, 0.7, 0.8
Ec	Eckert number	0.1, 0.3, 0.6
Sc	Schmidt number	0.1, 0.3, 5.0
N_b	Brownian motion parameter	0.1, 0.9, 1.5
N_t	Thermophoresis parameter	0.3, 0.5, 0.7
Df	Dufour parameter	0.1, 0.3, 0.5
m	Wall friction coefficient	1.0, 2.0, 3.0, 4.0

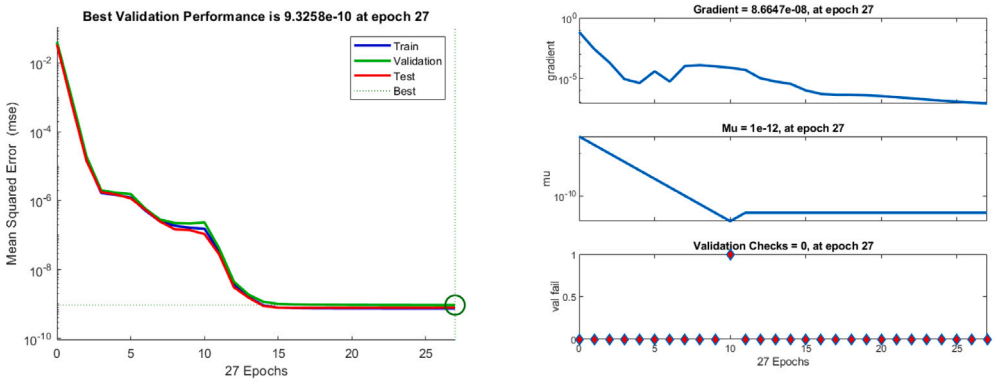

(a) Performance Plot

(b) Training State Plot

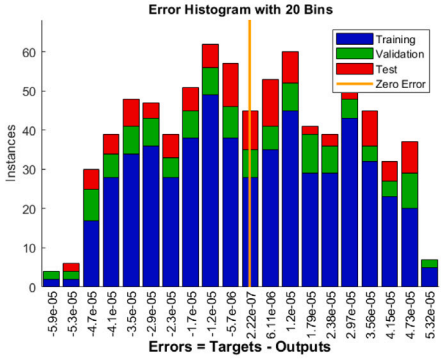

(c) Error Histogram

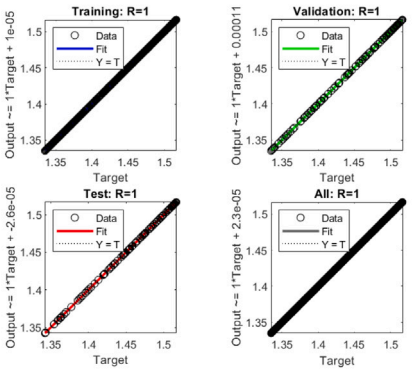

(d) Regression Plot

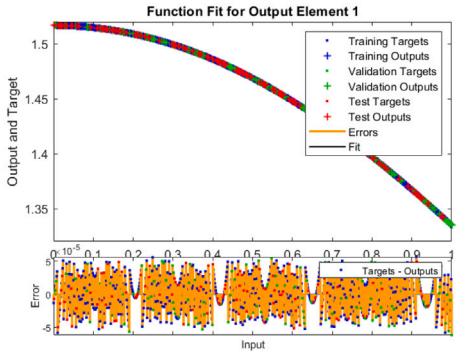

(e) Function fitting graph

Fig. 9. Effect of the Brownian diffusion number (Nb) on NN-LMB model predictions.

indicates the ratio of momentum to mass diffusivity. The Prandtl number (Pr) expresses the ratio of momentum to thermal diffusivity, and the radiation parameter (R) accounts for radiative heat transfer effects. The Eckert number (Ec) reflects viscous dissipation, relating the conversion of kinetic energy into internal energy. Collectively, these parameters define the combined influence of magnetic, thermal, and diffusive mechanisms within the Carreau nanofluid framework.

The influence of the inertial term, represented by the Reynolds number (Re), on the dimensionless velocity distribution $f(\xi)$ within converging and diverging channels is illustrated in Figs. 15 and 16, respectively. It is important to note that the flow rate is conserved in accordance with the imposed wall friction boundary conditions.

Fig. 15 reveals that, in the converging channel, an increase in Re enhances the velocity distribution. This effect arises from the dominance of inertial forces, which intensify with higher Reynolds numbers. Physically, the narrowing of the channel walls amplifies the pressure gradient, thereby accelerating the flow. Since the Reynolds number quantifies the ratio of inertial to viscous forces, an elevated Re corresponds to stronger inertia relative to viscosity. Consequently, greater inertial momentum combined with geometric contraction leads to a rise in the centerline velocity as well as in the overall outflow.

In contrast, Fig. 16 illustrates that in the diverging channel, an increase in the Reynolds number (Re) leads to a decline in the velocity distribution. This reduction is primarily attributed to the adverse action of inertial forces along the expanding channel walls, which oppose the forward motion of the fluid. As Re rises, the inertial dominance hinders the flow mobility, thereby lowering the velocity profile across the channel, with the effect being most significant near the centerline. Furthermore, at sufficiently large Re, the dimensionless velocity $f(\xi)$ approaches negative values, indicating the onset of flow reversal and the possible formation of a backflow/inflow zone within the diverging geometry.

The significant influence of the magnetic parameter (M) on the velocity profiles within converging and diverging channels is presented in Figs. 17 and 18, respectively. The results indicate that as M increases,

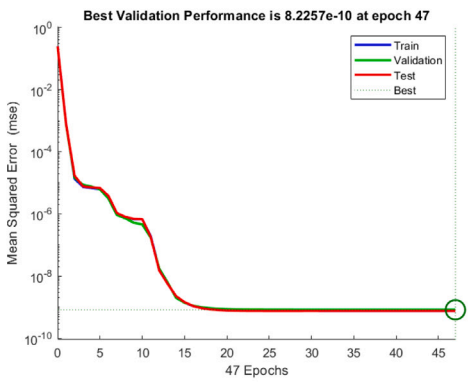

(a) Performance Plot

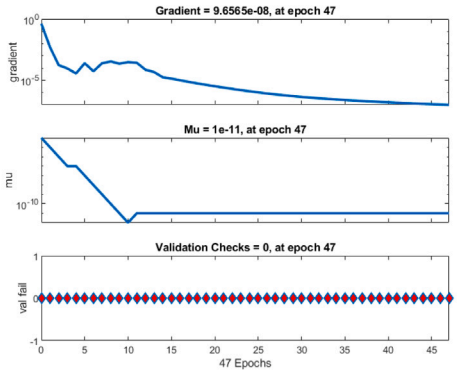

(b) Training State Plot

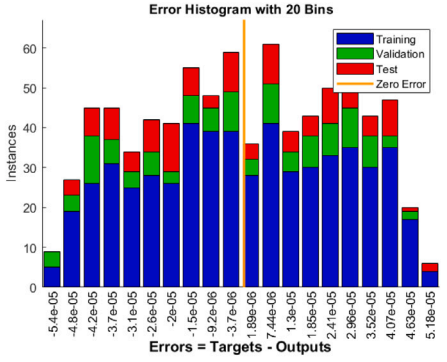

(c) Error Histogram

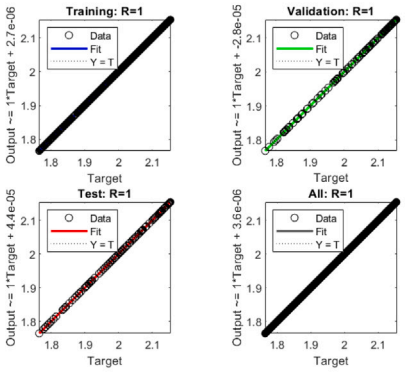

(d) Regression Plot

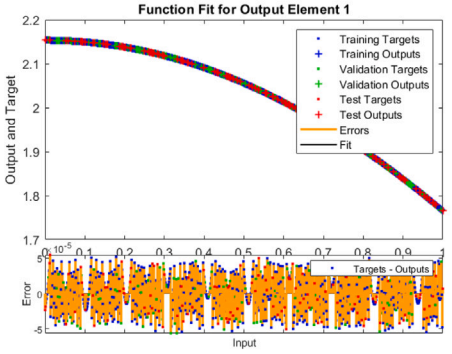

(e) Function fitting graph

Fig. 10. Effect of the thermophoresis parameter (Nt) on NN-LMB model predictions.

the velocity of the nanofluid rises in both channel configurations due to the enhanced action of the Lorentz force. In converging channels, fluid elements near the wall accelerate more rapidly than those along the centerline, leading to an overall increase in the velocity distribution. In diverging channels, the application of stronger magnetic forces counteracts the adverse pressure gradient, thereby suppressing flow separation and promoting smoother acceleration of the fluid.

At higher values of M, the magnetic influence becomes dominant, channeling the flow more effectively through the wedge geometry and supporting higher velocity magnitudes throughout the domain. This behavior underscores the constructive role of magnetic forces in improving flow mobility within both converging and diverging channels.

Figs. 19 and 20 illustrate the variation of nanofluid velocity within the channel under the influence of the wall friction coefficient ($m \geq 0$). The results highlight that surface roughness exerts a significant impact on the fluid motion. Since the pressure gradient of two-phase flow is a key parameter in the design and operation of nuclear power systems, accurate characterization of wall friction becomes indispensable for reliable channel flow modeling. In particular, the modeling of wall friction plays a vital role in assessing the performance of passive heat removal systems, which rely on two-phase natural circulation at relatively low velocities. Therefore, precise evaluation of wall friction effects across a wide range of operating conditions is crucial for the safety analysis of converging–diverging channel flows. In both converging and diverging geometries, the velocity of the nanofluid decreases as wall friction intensifies. Furthermore, an increase in the magnetic parameter enhances the Lorentz force, which strengthens the resistive forces opposing the flow and further suppresses the velocity distribution within the channel.

Figs. 21 and 22 illustrate the effect of the Prandtl number (Pr) on the temperature distribution for both channel configurations. As Pr

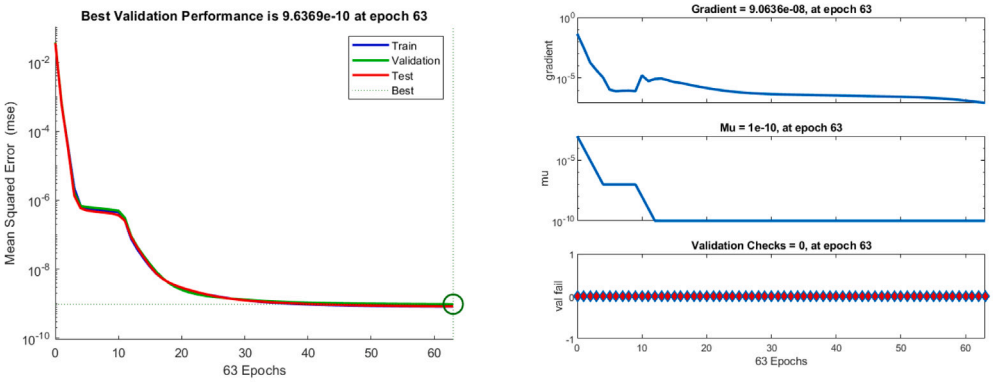

(a) Performance Plot

(b) Training State Plot

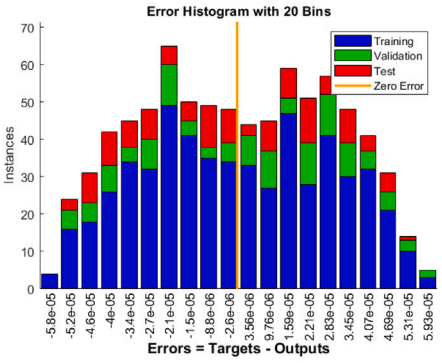

(c) Error Histogram

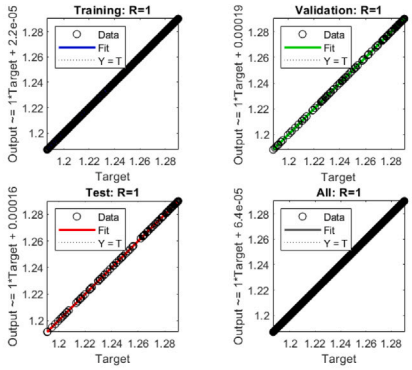

(d) Regression Plot

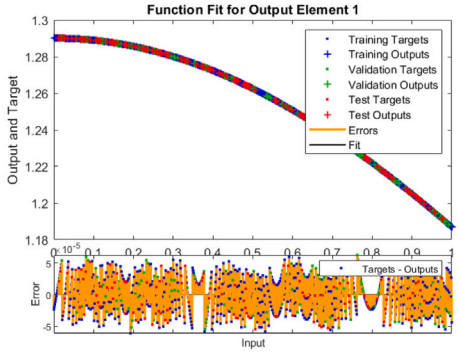

(e) Function fitting graph

Fig. 11. Effect of the radiation parameter (R) on NN-LMB model predictions.

increases, the temperature profile $\Theta(\eta)$ rises, and the thermal boundary layer becomes thinner. This behavior occurs because a higher Pr corresponds to a fluid with lower thermal diffusivity relative to momentum diffusivity, which reduces the rate at which heat is conducted away from the fluid. Consequently, thermal energy accumulates near the walls, elevating the local temperature.

In the wedge-type flow, increasing Pr reduces the thermal diffusivity of the fluid, which limits the spreading of heat away from the walls. As a result, thermal energy is retained within the boundary layer, leading to higher local temperatures and a thinner thermal layer. This effect is more pronounced near the walls, where the interplay between momentum and thermal diffusion directly governs the temperature profile. Thus, elevated Pr values intensify the temperature rise in both converging and diverging channel configurations, highlighting the inverse relationship between thermal diffusivity and the Prandtl number in controlling heat transport.

Figs. 23 and 24 illustrate the effect of the Brownian motion parameter (Nb) on the temperature distribution for both channel configurations. The results indicate that an increase in Nb intensifies the random motion of nanoparticles, which promotes enhanced energy transport from the fluid to the particles, thereby reducing the overall temperature of the flow. In the nanofluid model, the inherent Brownian motion of suspended nanoparticles significantly influences both the thermal and momentum fields, playing a key role in determining the heat transfer characteristics of the system.

Thermophoresis refers to the migration of nanoparticles induced by temperature gradients. As depicted in Figs. 25 and 26, this mechanism enhances the drift of the suspended particles, which in turn elevates the fluid temperature across the flow domain for both configurations. From a physical standpoint, the thermophoresis parameter (Nt) governs the intensity of the thermophoretic force that transports nanoparticles from regions of higher temperature towards cooler zones. This particle redistribution augments the thermal energy content of the fluid, thereby

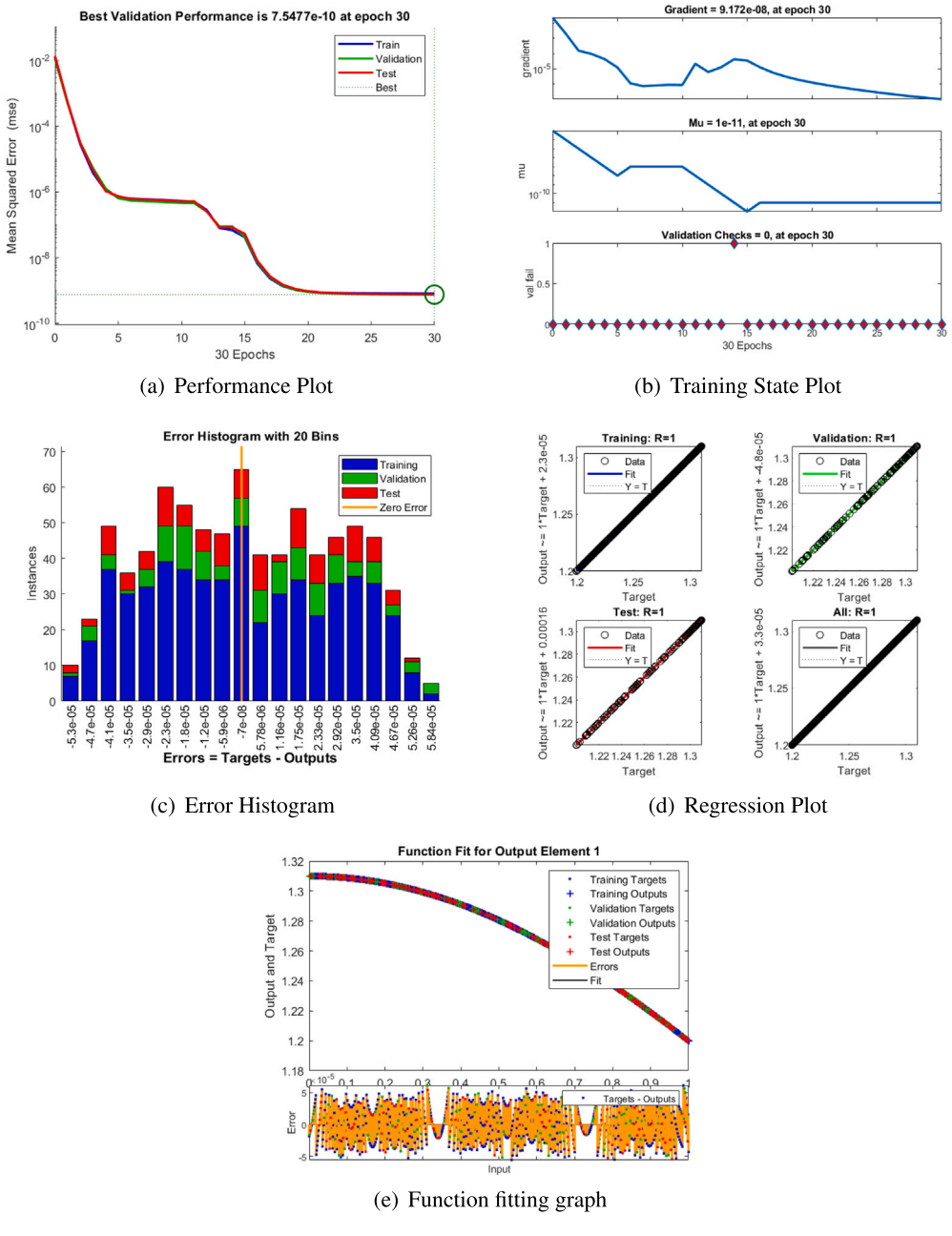

(a) Performance Plot

(b) Training State Plot

(c) Error Histogram

(d) Regression Plot

(e) Function fitting graph

Fig. 12. Effect of the Dufour number (Df) on NN-LMB model predictions.

enriching the temperature field and thickening the thermal boundary layer.

Figs. 27 and 28 depict the influence of the radiation parameter (R) on the temperature distribution for both channel configurations. It is evident that as R increases, the temperature profile $\Theta(\eta)$ decreases, accompanied by a reduction in the thermal boundary layer thickness. Physically, higher values of R enhance radiative heat loss from the fluid, diminishing the local energy content and leading to lower temperatures.

A comparative assessment indicates that this cooling effect is more pronounced in the diverging channel than in the converging one. The wider geometry of the divergent configuration allows for more efficient thermal dissipation, whereas the converging channel, constrained by a smaller opening and the presence of nanoparticles, resists heat loss, resulting in a comparatively smaller reduction in temperature. Therefore, increasing radiation selectively intensifies the cooling in the divergent channel while exerting a weaker effect in the convergent configuration.

Figs. 29 and 30 present the temperature field distributions for varying values of the Dufour number (Df) in both channel configurations. The results indicate that as Df is augmented, the fluid temperature rises correspondingly in both cases. The effect is particularly dominant in the divergent channel, where the thermal enhancement is more pronounced compared to the converging channel. This trend highlights the influence of the diffusion–thermo mechanism, represented by the Dufour coefficient.

The Dufour effect, also referred to as the diffusion–thermo effect, arises when a concentration gradient generates an associated energy flux. With higher Df, energy transport is reinforced, leading to a reduction in the thermal gradient and a noticeable elevation of the overall temperature field. From a physical perspective, the increase in Df intensifies the heat flux driven by concentration differences, thereby

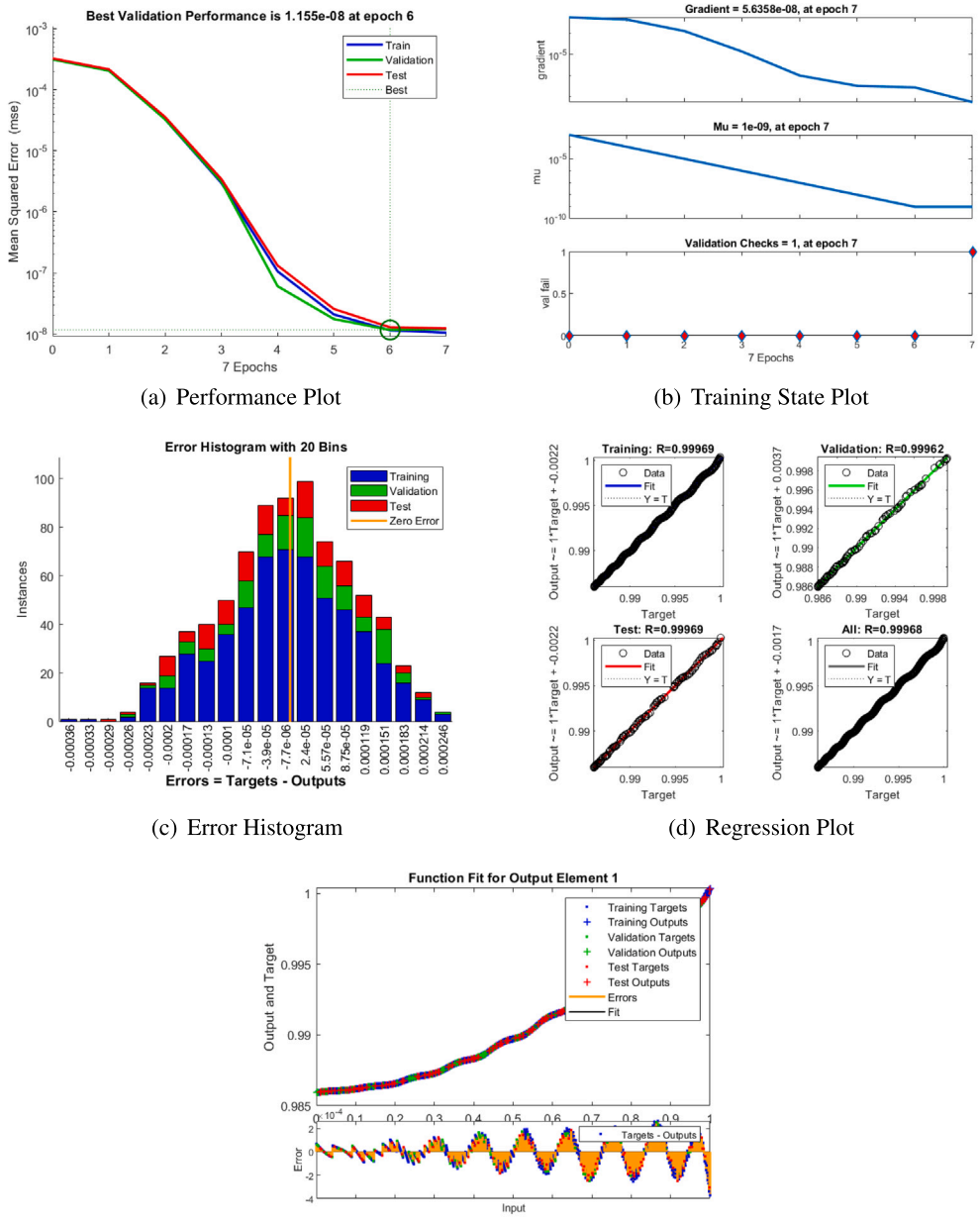

(a) Performance Plot (b) Training State Plot

(c) Error Histogram (d) Regression Plot

(e) Function fitting graph

Fig. 13. Effect of the Schmidt number (Sc) on NN-LMB model predictions.

enriching the thermal response of the fluid and promoting stronger temperature growth within the channel.

The effect of the magnetic parameter M on the temperature profile $\Theta(\xi)$ is presented in Figs. 31 and 32 for both configurations. The magnetic parameter characterizes the balance between electromagnetic and viscous forces. Physically, as the magnetic field strengthens, the induced electric vortices in the flow become more dominant. These vortices oppose the fluid motion, enhancing the resistive forces acting on the fluid. The resulting impedance produces additional friction, which increases viscous dissipation within the boundary layer. This dissipation manifests as heat, thereby raising the temperature of the fluid. Consequently, for both convergent and divergent channels, the temperature profile shows a monotonic increase with higher magnetic parameter M. The Lorentz force induced by the applied magnetic field thus plays a central role in enhancing internal resistance and promoting greater heat generation in the fluid.

The concentration profile $\Psi(\xi)$ is depicted against the Schmidt number Sc in Figs. 33 and 34, showing noticeable variation for both convergent ($\beta = -30°$) and divergent ($\beta = 30°$) channel configurations. The Schmidt number Sc represents the ratio of momentum diffusivity to mass diffusivity, and it is inversely related to the molecular diffusivity D_B. An increase in Sc implies reduced mass diffusivity, which manifests as a decline in the concentration field. When Sc < 1, momentum diffusivity dominates over mass diffusivity, altering the relative transport processes within the channel. This distinction becomes more evident in convergent and divergent geometries, where reduced momentum diffusivity enhances nanoparticle concentration. Physically, as Sc increases, the suppression of mass diffusion leads to a progressive reduction in nanoparticle concentration. This effect is particularly strong near the

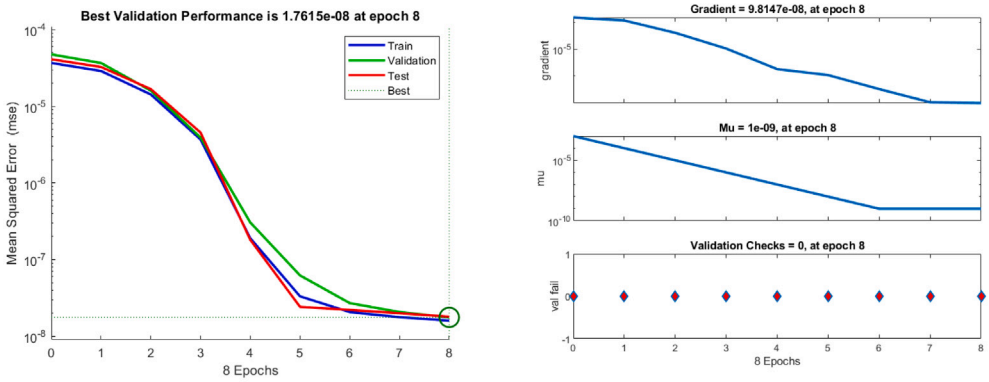

(a) Performance Plot (b) Training State Plot

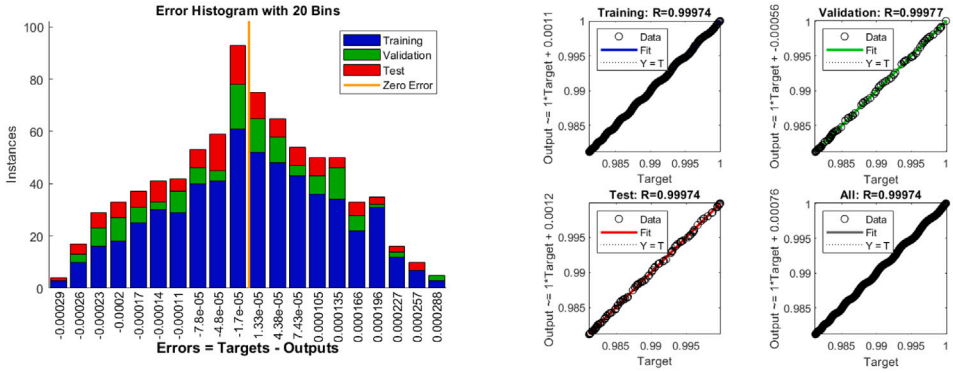

(c) Error Histogram (d) Regression Plot

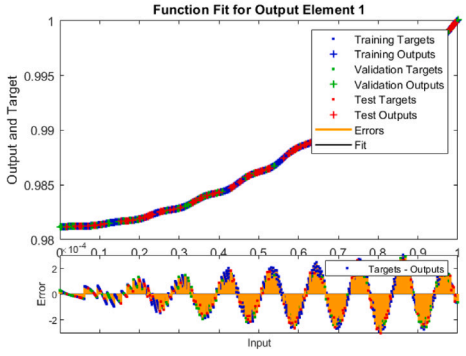

(e) Function fitting graph

Fig. 14. Effect of the Eckert number (Ec) on NN-LMB model predictions.

central region of the channel, where sharp concentration gradients appear due to intensified viscous forces acting on the flow.

The concentration profile $\Psi(\xi)$ is illustrated against the Eckert number Ec in Figs. 35 and 36, where a clear decreasing trend is observed for both convergent ($\beta = -30°$) and divergent ($\beta = 30°$) channels. Physically, the Eckert number signifies the influence of viscous dissipation relative to enthalpy. As Ec increases, viscous heating becomes dominant, which elevates the thermal energy of the fluid and reduces the nanoparticle concentration through enhanced thermal agitation. Consequently, the concentration field $\Psi(\xi)$ demonstrates a marked decline with increasing Ec, more pronounced near the central region of the channel due to stronger viscous effects.

The physical insights derived from the variation of key parameters possess significant engineering and industrial relevance. The magnetic parameter (M) demonstrates the potential for magnetic field–based flow control and localized heating, which is useful in electromagnetic pumps and metallurgical cooling systems. The Reynolds number (Re) and Weissenberg number (We) reveal the combined influence of inertial and elastic effects, relevant to polymeric fluid processing and biofluid transport applications. The Prandtl number (Pr) and radiation parameter (R) govern thermal diffusion and radiative heat transfer, providing guidelines for optimizing heat exchangers and energy recovery devices. The Eckert number (Ec) links viscous dissipation to internal energy conversion, which is critical in high-speed lubrication and thermal

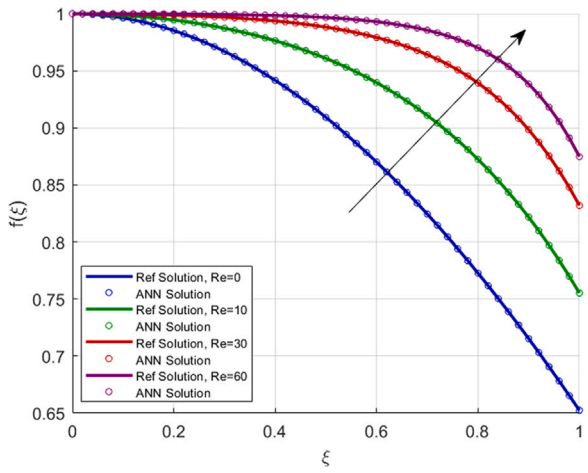

Fig. 15. Velocity in a convergent channel at $\beta = -30°$ for varying Re.

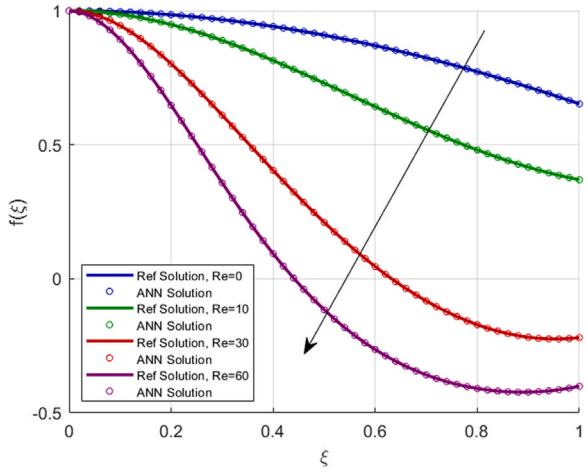

Fig. 16. Velocity in a divergent channel at $\beta = 30°$ for varying Re.

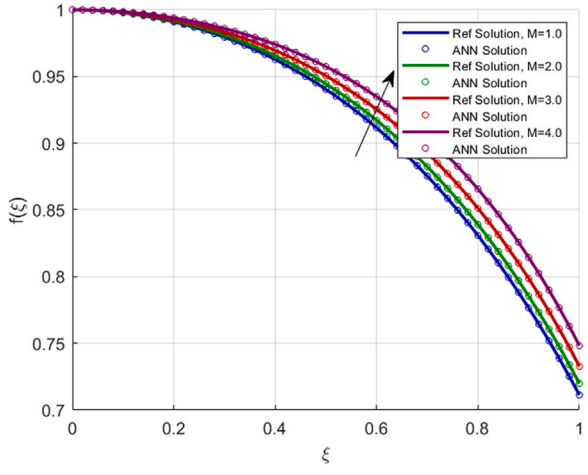

Fig. 17. Velocity in a convergent channel at $\beta = -30°$ for varying M.

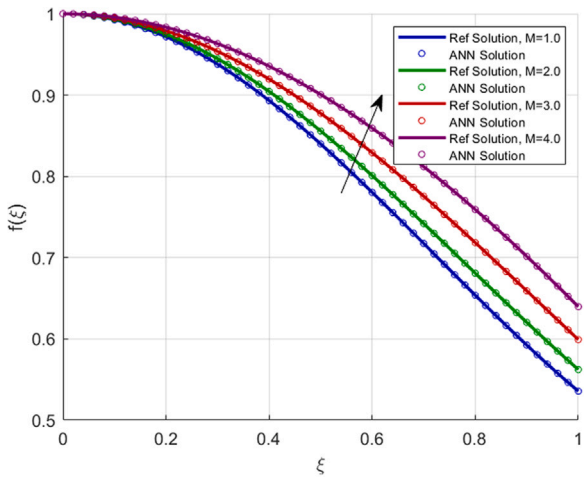

Fig. 18. Velocity in a divergent channel at $\beta = 30°$ for varying M.

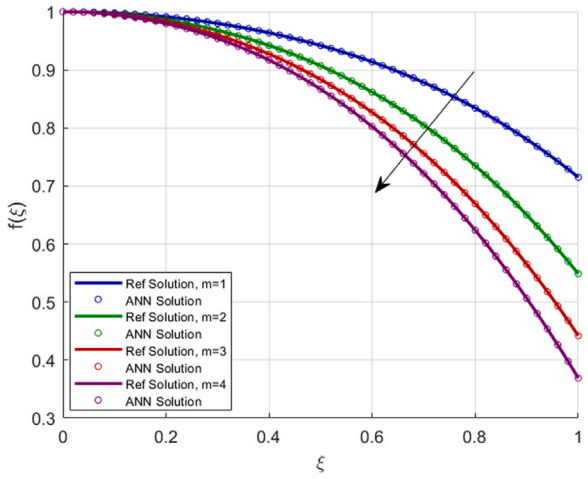

Fig. 19. Velocity in a convergent channel at $\beta = -30°$ for varying m.

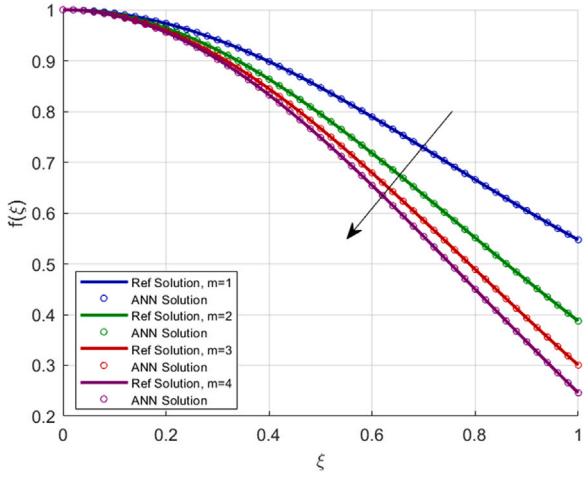

Fig. 20. Velocity in a divergent channel at $\beta = 30°$ for varying m.

management systems. Similarly, the Schmidt number (Sc), Brownian motion parameter (N_b), thermophoresis parameter (N_t), and Dufour number (Df) contribute to understanding nanoparticle mass transport in microchannel cooling and biomedical fluid flows. The temperature slip parameter (A) and wall friction coefficient (m) illustrate boundary stress effects that can guide surface treatment or coating designs for drag reduction and thermal control. Collectively, these findings

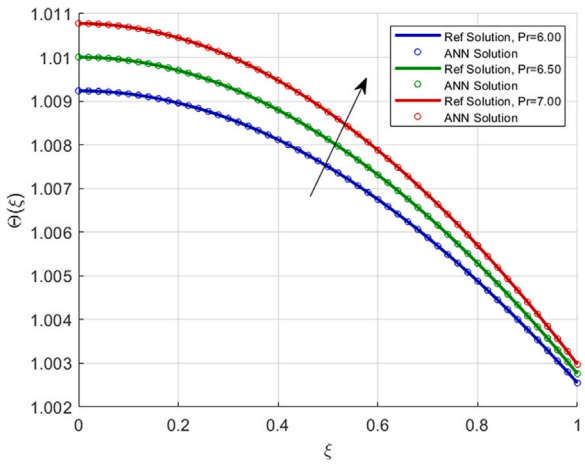

Fig. 21. Temperature profile in a convergent channel at $\beta = -30°$ for varying Pr.

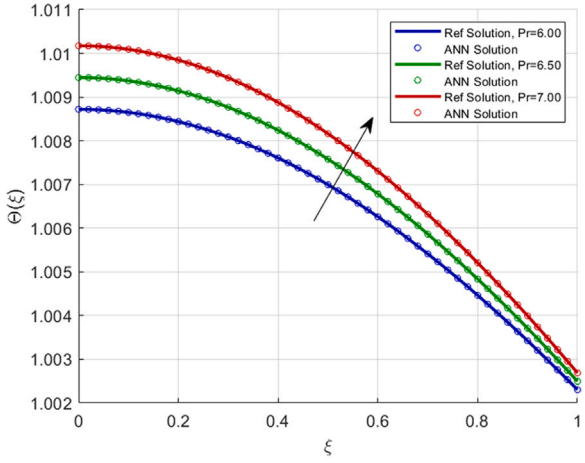

Fig. 22. Temperature profile in a divergent channel at $\beta = 30°$ for varying Pr.

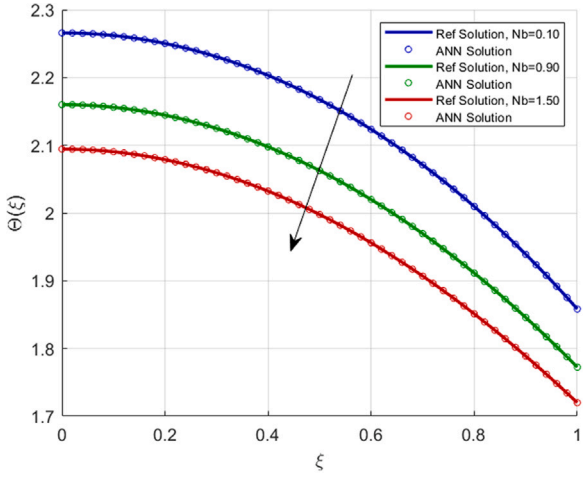

Fig. 23. Temperature profile in a convergent channel at $\beta = -30°$ for varying Nb.

underline the applicability of the present Carreau nanofluid model in advanced microfluidic, energy, and cooling technologies.

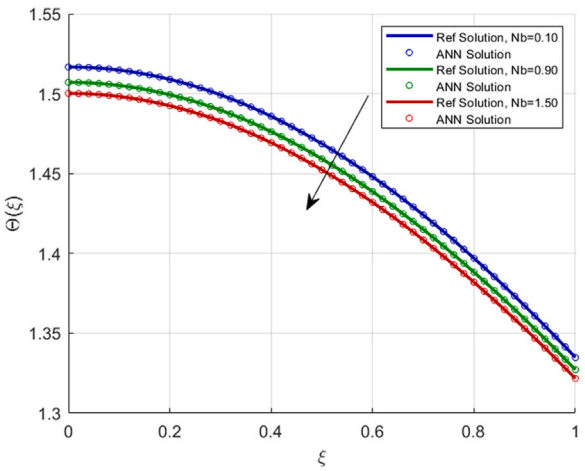

Fig. 24. Temperature profile in a divergent channel at $\beta = 30°$ for varying Nb.

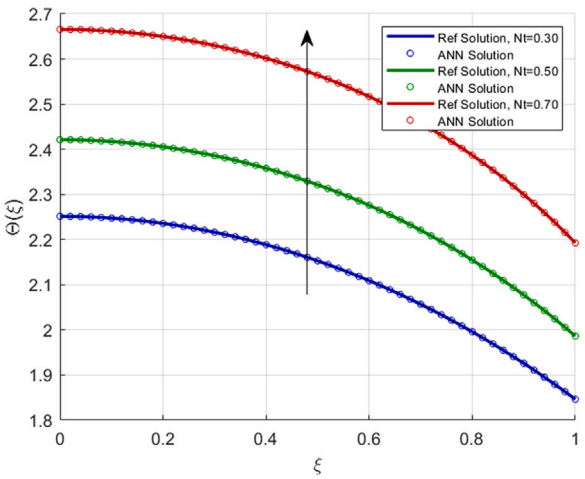

Fig. 25. Temperature profile in a convergent channel at $\beta = -30°$ for varying Nt.

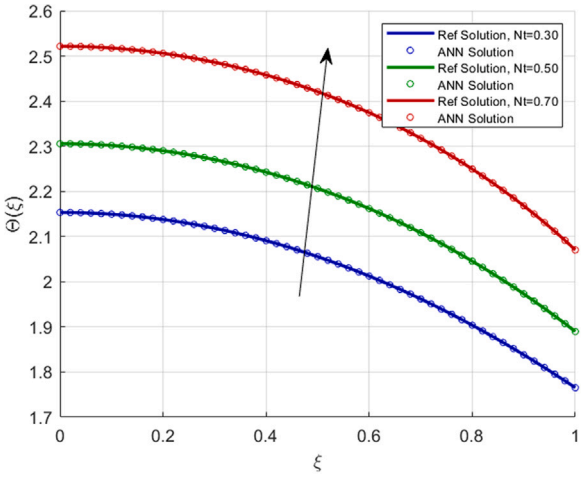

Fig. 26. Temperature profile in a divergent channel at $\beta = 30°$ for varying Nt.

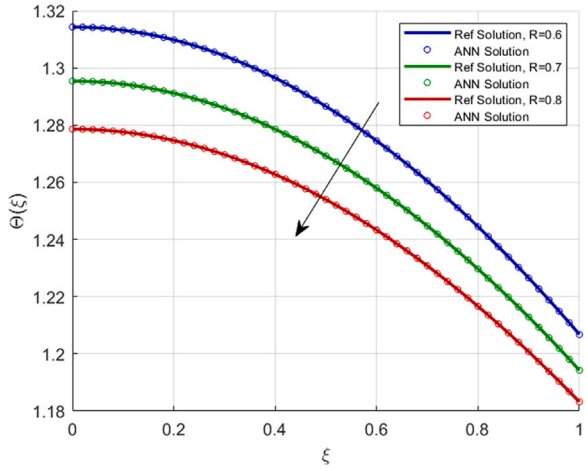

Fig. 27. Temperature profile in a convergent channel at $\beta = -30°$ for varying R.

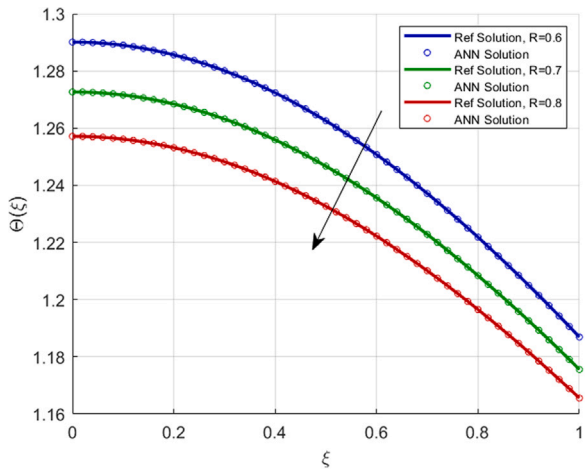

Fig. 28. Temperature profile in a divergent channel at $\beta = 30°$ for varying R.

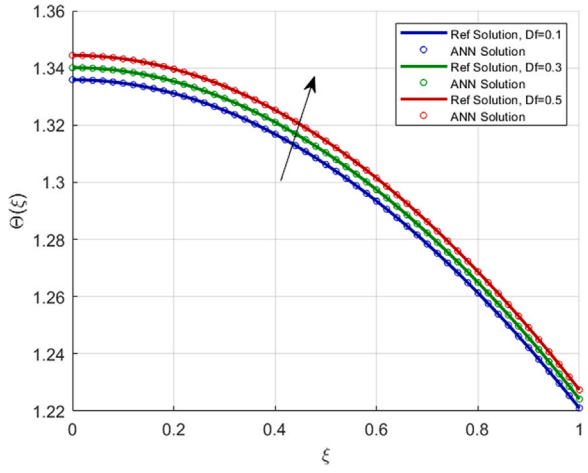

Fig. 29. Temperature profile in a convergent channel at $\beta = -30°$ for varying Df.

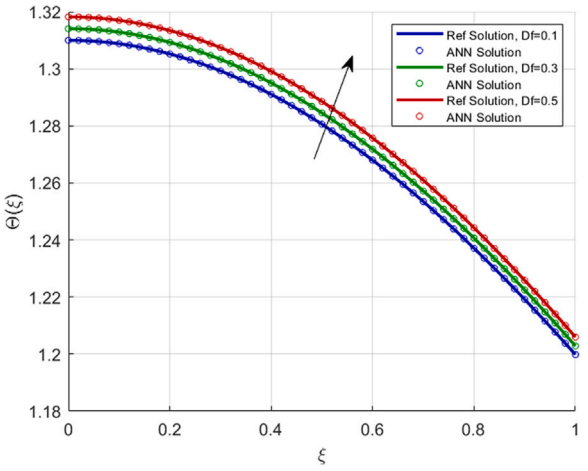

Fig. 30. Temperature profile in a divergent channel at $\beta = 30°$ for varying Df.

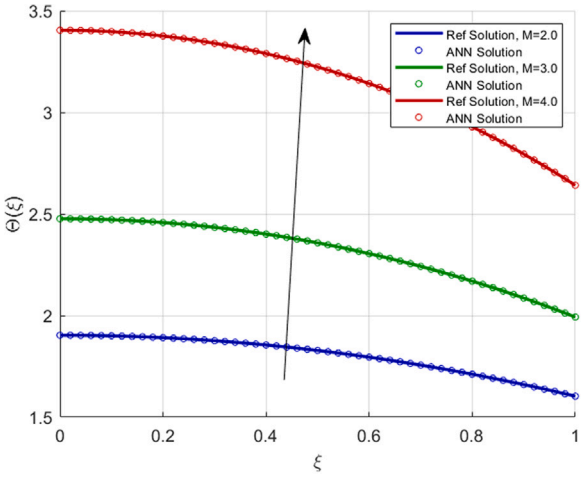

Fig. 31. Temperature profile in a convergent channel at $\beta = -30°$ for varying M.

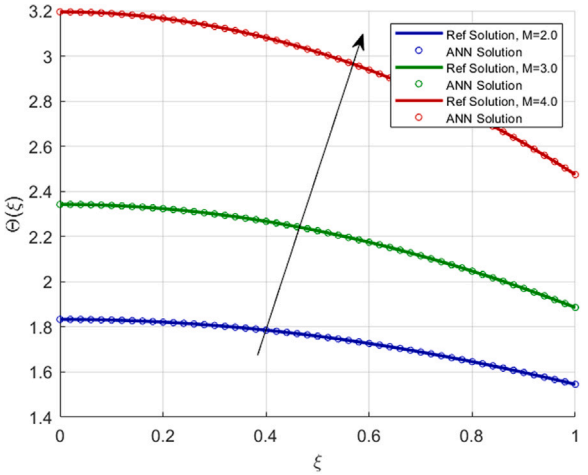

Fig. 32. Temperature profile in a divergent channel at $\beta = 30°$ for varying M.

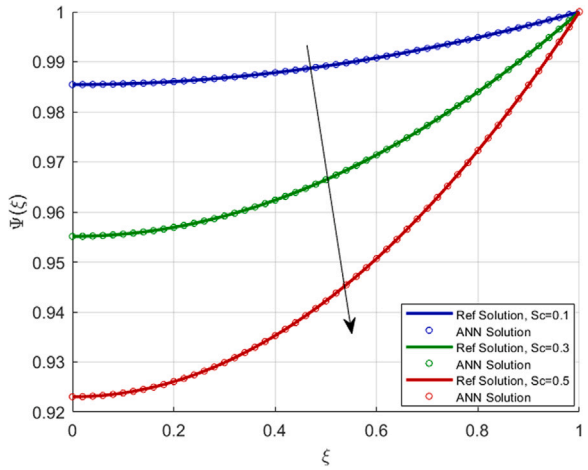

Fig. 33. Concentration profile in a convergent channel at $\beta = -30°$ for varying Sc.

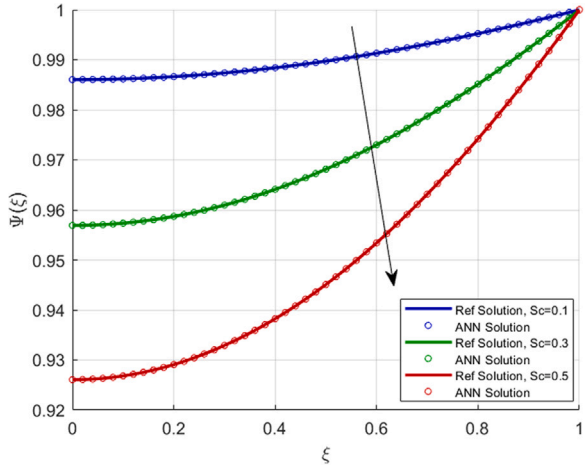

Fig. 34. Concentration profile in a divergent channel at $\beta = 30°$ for varying Sc.

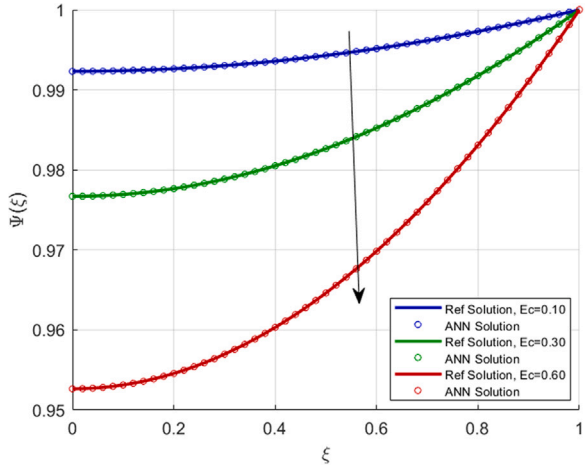

Fig. 35. Concentration profile in a convergent channel at $\beta = -30°$ for varying Ec.

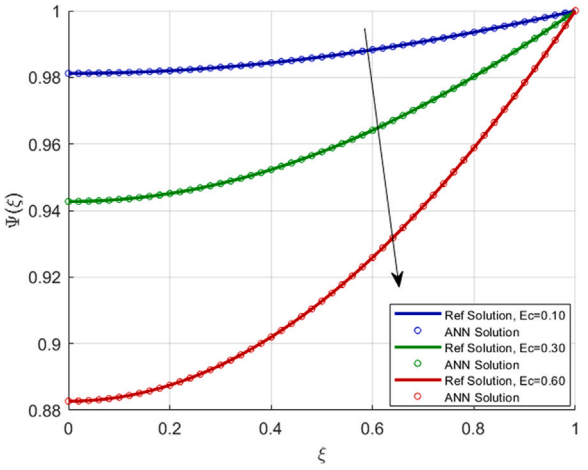

Fig. 36. Concentration profile in a divergent channel at $\beta = 30°$ for varying Ec.

A comparative assessment with existing literature further validates the accuracy and efficiency of the proposed NN–LMB-based Carreau nanofluid model. Rehman et al. [50] examined MHD flow between convergent and divergent channels by considering entropy production and Dufour–Soret effects using conventional numerical techniques, while Rehman et al. [51] explored non-Newtonian nanofluid flow with wall slip effects through purely computational approaches. Similarly, Asghar et al. [52] and Garimella et al. [53] investigated Jeffery–Hamel and shear-thinning fluid flows numerically, highlighting challenges in achieving stable convergence for complex nonlinear systems. Hayat et al. [54] also utilized finite difference analysis for Casson fluid flows but reported limited flexibility in handling multi-parameter variations. In contrast, the present NN–LMB framework demonstrates superior convergence stability, reduced computational effort, and enhanced generalization across a wide range of governing parameters. These advantages underscore the capability of the NN–LMB approach to capture nonlinear magnetohydrodynamic behavior in convergent–divergent geometries more efficiently than traditional numerical solvers.

5. Conclusion

This study examined non-Newtonian Carreau nanofluid flow through wedge-shaped convergent and divergent channels under magnetic field, thermal radiation, and viscous dissipation. The governing PDEs were transformed into ODEs using similarity transformations and solved via MATLAB's `bvp4c`. The resulting solutions trained a feedforward NN-LMB model for accurate prediction of velocity, temperature, and nanoparticle concentration profiles.

- The NN-LMB model used 70% training, 15% validation, and 15% testing, achieving high accuracy with the minimum validation MSE of 7.55×10^{-10} and regression coefficient $R \approx 1$, confirming reliable generalization.
- Magnetic parameter (M) enhanced velocity and temperature through the Lorentz force and viscous dissipation.
- Reynolds number (Re) increased velocity in converging channels but reduced it in diverging channels due to adverse inertia.
- Wall friction coefficient (m) suppressed velocity, while Prandtl number (Pr) enhances the temperature and Brownian motion (Nb) diminishing the overall temperature of the stream.

Table 6
List of symbols, definitions, and corresponding units.

Symbol	Definition	Unit
U_r	Radial velocity component	m/s
T	Temperature	K
C	Nanoparticle concentration	kg/m^3
T_w, C_w	Wall temperature and concentration	K, kg/m^3
B_0	Magnetic field strength	T
ρ_f	Base fluid density	kg/m^3
μ_0	Dynamic viscosity	Pa s
ν_f	Kinematic viscosity	m^2/s
k_f	Thermal conductivity	W/(m K)
c_p	Specific heat at constant pressure	J/(kg K)
σ	Electrical conductivity	S/m
σ^*	Stefan–Boltzmann constant	W/(m^2 K^4)
k^*	Mean absorption coefficient	m^{-1}
D_B	Brownian diffusion coefficient	m^2/s
D_T	Thermophoretic diffusion coefficient	m^2/s
K_T	Thermal diffusion ratio	–
β	Half-angle of the wedge channel	rad
γ	Wall friction coefficient	–
δ	Temperature slip factor	–
Π	Consistency index (Carreau model)	–
n	Power-law index (Carreau model)	–
Q	Volumetric flow rate	m^3/s
M	Magnetic parameter	–
Re	Reynolds number	–
We	Weissenberg number	–
Pr	Prandtl number	–
R	Radiation parameter	–
Ec	Eckert number	–
Sc	Schmidt number	–
N_b	Brownian motion parameter	–
N_t	Thermophoresis parameter	–
Df	Dufour parameter	–
A	Temperature slip parameter	–
m	Wall friction coefficient (dimensionless)	–

- Thermophoresis (Nt and Dufour number (Df) increased temperature, with divergence amplifying the effects.
- Schmidt number (Sc) and Eckert number (Ec) decreased nanoparticle concentration via reduced mass diffusion and enhanced viscous heating.

Overall, the bvp4c–NN-LMB framework offers a fast and accurate approach for modeling nonlinear Carreau nanofluid transport in convergent and divergent channels, applicable to microscale and industrial thermal systems. Future research may consider unsteady and three-dimensional flow cases, hybrid nanofluid models, and integration of advanced deep learning methods such as PINNs to further improve predictive accuracy and practical relevance.

A comprehensive list of all symbols, parameters, and variables employed in this study is provided in nomenclature Table 6. The table includes their physical meanings and corresponding SI units to enhance clarity and facilitate better understanding of the mathematical formulation and results.

CRediT authorship contribution statement

Saraj Khan: Writing – original draft, Methodology, Investigation, Data curation, Conceptualization. **Muhammad Imran Asjad:** Writing – review & editing, Supervision, Project administration, Methodology, Investigation, Conceptualization. **Muhammad Naeem Aslam:** Visualization, Software, Formal analysis. **Marei S. Alqarni:** Writing – review & editing, Validation, Resources, Funding acquisition.

Declaration of competing interest

The authors declare that they have no known competing financial interests or personal relationships that could have appeared to influence the work reported in this paper.

Acknowledgments

The authors extend their appreciation to the Deanship of Research and Graduate Studies at King Khalid University, KSA, Saudi Arabia for funding this work through Large Research Project under grant number RGP.2/202/46.

Data availability

No data was used for the research described in the article.

References

[1] J.A. Shercliff, A Textbook of Magnetohydrodynamics, Pergamon Press, 1965.
[2] K.R. Cramer, S.I. Pai, Magnetofluid Dynamics for Engineers and Applied Physicists, Krieger Publishing Company, 2005.
[3] I. Pop, D.B. Ingham, Convective Heat Transfer: Mathematical and Computational Modelling of Viscous Fluids and Porous Media, Pergamon, 2004.
[4] S.U.S. Choi, Enhancing thermal conductivity of fluids with nanoparticles, ASME Int. Mech. Eng. Congr. Expo. (1995) 99–105.
[5] R.B. Bird, R.C. Armstrong, O. Hassager, Dynamics of Polymeric Liquids, Volume 1: Fluid Mechanics, second ed., Wiley, 1987.
[6] A.M. Afonso, M.S.N. Oliveira, P.J. Oliveira, M.A. Alves, F.T. Pinho, The finite volume method in computational rheology, Finite-Volume Methods–Powerful Means Eng. Des. (2012) 141–170.
[7] P.J. Carreau, Rheological equations from molecular network theories, *Trans. Soc. Rheol.* 16 (1) (1972) 99–127.
[8] M. Khan, Hashim, Axisymmetric flow and heat transfer of the Carreau fluid due to a radially stretching sheet: Numerical study, J. Appl. Mech. Tech. Phys. 58 (3) (2017) 410–418.
[9] A. Bejan, Entropy generation minimization: The new thermodynamics of finite-size devices and finite-time processes, J. Appl. Phys. 79 (3) (1996) 1191–1218.
[10] M.M. Rashidi, M. Nasiri, M.S. Shadloo, Z. Yang, Entropy generation in a circular tube heat exchanger using nanofluids: Effects of different modeling approaches, Heat Transf. Eng. 38 (9) (2017) 853–866.

[11] A.Z. Sahin, R. Ben-Mansour, Entropy generation in laminar fluid flow through a circular pipe, Entropy 5 (5) (2003) 404–416.
[12] P.A. Davidson, Introduction to Magnetohydrodynamics, second ed., Cambridge University Press, 2016.
[13] S.M. Seyyedi, A.S. Dogonchi, M. Hashemi-Tilehnoee, M. Waqas, D.D. Ganji, Entropy generation and economic analyses in a nanofluid filled L-shaped enclosure subjected to an oriented magnetic field, Appl. Therm. Eng. 168 (2020) 114789.
[14] S.A.M. Mehryan, M. Izadi, A.J. Chamkha, M.A. Sheremet, Natural convection and entropy generation of a ferrofluid in a square enclosure under the effect of a horizontal periodic magnetic field, J. Mol. Liq. 263 (2018) 510–525.
[15] A. Bejan, Entropy Generation Minimization: The Method of Thermodynamic Optimization of Finite-Size Systems and Finite-Time Processes, Revised ed., CRC Press, 2013.
[16] O. Mahian, A. Kianifar, S. Wongwises, A.J. Chamkha, I. Pop, C. Kleinstreuer, Analysis of entropy generation in nanofluid flow, Int. J. Heat Mass Transfer 65 (2013) 514–532.
[17] A.J. Chamkha, Coupled heat and mass transfer by natural convection about a truncated cone in the presence of magnetic field and thermal radiation effects, Heat Mass Transf. 40 (2004) 835–841.
[18] N. Khan, I. Riaz, M.S. Hashmi, S.A. Musmar, S.U. Khan, Z. Abdelmalek, I. Tlili, Aspects of chemical entropy generation in flow of casson nanofluid between radiative stretching disks, Entropy 22 (5) (2020) 495.
[19] T. Hayat, S.A. Khan, M.I. Khan, A. Alsaedi, Theoretical investigation of ree-eyring nanofluid flow with entropy optimization and arrhenius activation energy between two rotating disks, Comput. Methods Programs Biomed. 177 (2019) 57–68.
[20] O.D. Makinde, Entropy-generation analysis for variable-viscosity channel flow with non-uniform wall temperature, Appl. Energy 85 (5) (2008) 384–393.
[21] O. Makinde, O. Bég, On inherent irreversibility in a reactive hydromagnetic channel flow, J. Therm. Sci. 19 (1) (2010) 72–79.
[22] G.B. Jeffery, The two-dimensional steady motion of a viscous fluid, Lond. Edinb. Dublin Philos. Mag. J. Sci. 29 (172) (1915) 455–465.
[23] G. Hamel, Spiralförmige Bewegungen zäher Flüssigkeiten, Jahresber. der Dtsch. Mathematiker-Vereinigung 25 (1917) 34–60.
[24] J. Nagler, Jeffery-Hamel flow of nano fluid influenced by wall slip conditions, J. Nanofluids 5 (6) (2016) 960–967.
[25] M.S. Alam, M.A.H. Khan, O.D. Makinde, Magneto-nanofluid dynamics in convergent-divergent channel and its inherent irreversibility, Defect Diffus. Forum 377 (2017) 95–110.
[26] M. Khan, F. Sultan, T. Hayat, A. Alsaedi, Soret and dufour effects on MHD flow of williamson fluid over a rotating disk with anisotropic slip, Results Phys. 6 (2016) 917–924.
[27] S. Qayyum, T. Hayat, M.I. Khan, M.I. Khan, A. Alsaedi, Optimization of entropy generation and dissipative nonlinear radiative Von Karman's swirling flow with Soret and Dufour effects, J. Mol. Liq. 262 (2018) 261–274.
[28] I.H. Qureshi, M. Nawaz, M.A. Abdel-Sattar, S. Aly, M. Awais, Numerical study of heat and mass transfer in MHD flow of nanofluid in a porous medium with Soret and Dufour effects, Heat Transfer—Asian Res. 50 (5) (2021) 4501–4515.
[29] K. Ramesh, D. Patidar, O. Ojjela, Entropy generation analysis of free convection radiative MHD eyring–Powell fluid flow between porous parallel plates with Soret and Dufour effects, Heat Transfer—Asian Res. 50 (7) (2021) 6935–6954.
[30] M.N. Aslam, N. Shaukat, A. Riaz, I. Khan, S. Niazai, RETRACTED ARTICLE: Machine learning intelligent based hydromagnetic thermal transport under Soret and Dufour effects in convergent/divergent channels: a hybrid evolutionary numerical algorithm, Sci. Rep. 13 (1) (2023) 21973.
[31] S.I. Abdelsalam, K.S. Mekheimer, A.Z. Zaher, Dynamism of a hybrid Casson nanofluid with laser radiation and chemical reaction through sinusoidal channels, Waves Random Complex Media 35 (3) (2025) 4191–4212.
[32] V. Sridhar, K. Ramesh, M. Gnaneswara Reddy, M.N. Azese, S.I. Abdelsalam, On the entropy optimization of hemodynamic peristaltic pumping of a nanofluid with geometry effects, Waves Random Complex Media 35 (3) (2025) 4403–4423.
[33] S. Abdelsalam, P.P. Kumar, S. Balakrishnan, A. Magesh, P. Tamizharasi, Numerical treatment of entropy generation and bejan number into an electroosmotically-driven flow of sutterby nanofluid in an asymmetric microchannel, 2024.
[34] S.I. Abdelsalam, N. Alsedais, A.M. Aly, Revolutionizing bioconvection: Artificial intelligence-powered nano-encapsulation with oxytactic microorganisms, Eng. Appl. Artif. Intell. 137 (2024) 109128.
[35] S.I. Abdelsalam, A. Magesh, P. Tamizharasi, Optimizing fluid dynamics: An in-depth study for nano-biomedical applications with a heat source, J. Therm. Anal. Calorim. 150 (4) (2025) 2781–2793.
[36] S.I. Abdelsalam, M.M. Bhatti, Synergistic progression of nanoparticle dynamics in stenosed arteries, Qual. Theory Dyn. Syst. 24 (1) (2025) 6.
[37] N. Alsedais, M.A. Mansour, A.M. Aly, S.I. Abdelsalam, Artificial neural network validation of MHD natural bioconvection in a square enclosure: entropic analysis and optimization, Acta Mech. Sin. 41 (9) (2025) 724507.
[38] N. Elsedais, M.A. Mansour, A.M. Aly, S. Abdelsalam, Artificial intelligence-driven FVM-ANN model for entropy analysis of MHD natural bioconvection in nanofluid-filled porous cavities, 2024.
[39] S.I. Abdelsalam, M.A. Dagher, Y. Abd Elmaboud, A. Abdellateef, Towards understanding thermal management in unsteady boundary layer flow with AC/DC electric fields, Propuls. Power Res. 14 (1) (2025) 64–75.
[40] T. Oreyeni, A. Oladimeji Akindele, A. Martins Obalalu, S. Olakunle Salawu, K. Ramesh, Thermal performance of radiative magnetohydrodynamic Oldroyd-B hybrid nanofluid with Cattaneo–Christov heat flux model: Solar-powered ship application, Numer. Heat Transf. Part A: Appl. 85 (12) (2024) 1954–1972.
[41] M. Nazeer, F. Hussain, S. Iftikhar, M. Ijaz Khan, K. Ramesh, N. Shehzad, A. Baig, S. Kadry, Y.-M. Chu, Mathematical modeling of bio-magnetic fluid bounded within ciliated walls of wavy channel, Numer. Methods Partial Differential Equations 40 (2) (2024) e22763.
[42] K. Ramesh, A.S. Warke, K. Kotecha, K. Vajravelu, Numerical and artificial neural network modelling of magnetorheological radiative hybrid nanofluid flow with Joule heating effects, J. Magn. Magn. Mater. 570 (2023) 170552.
[43] D. Kumar, K. Ramesh, S. Chandok, Mathematical modeling and simulation for the flow of magneto-Powell-Eyring fluid in an annulus with concentric rotating cylinders, Chinese J. Phys. 65 (2020) 187–197.
[44] M.A.Z. Raja, R. Tabassum, E.R. El-Zahar, M. Shoaib, M.I. Khan, M.Y. Malik, S.U. Khan, S. Qayyum, Intelligent computing through neural networks for entropy generation in MHD third grade nanofluid under chemical reaction and viscous dissipation, Waves Random Complex Media (2022) 1–25.
[45] M. Shoaib, S. Naz, M.A.Z. Raja, R. Khanam, I. Ahmad, K.S. Nisar, Entropy generation in Reiner-Rivlin fluid flow under soret and dufour impact: Neural networks applications, Internat. J. Theoret. Phys. 64 (6) (2025) 170.
[46] K. Hornik, M. Stinchcombe, H. White, Multilayer feedforward networks are universal approximators, Neural Netw. 2 (5) (1989) 359–366.
[47] T.-H. Zhao, M.I. Khan, Y.-M. Chu, Artificial neural networking (ANN) analysis for heat and entropy generation in flow of non-Newtonian fluid between two rotating disks, Math. Methods Appl. Sci. 46 (3) (2023) 3012–3030.
[48] M. Elayarani, M. Shanmugapriya, Artificial neural network modeling of MHD stagnation point flow and heat transfer towards a porous stretching sheet, in: Aip Conference Proceedings, vol. 2161, (1) AIP Publishing LLC, 2019, 020043.
[49] E. Ghaderi, M. Bijarchi, S.K. Hannani, A. Nouri-Borujerdi, Evaluating joule heating influence on heat transfer and entropy generation in MHD channel flow: A parametric study and ill-posed problem solution using PINNs, 2024, arXiv preprint arXiv:2406.15810.
[50] S. Rehman, Hashim, S.B.H. Hassine, E. Tag Eldin, S.O. Shah, Investigation of entropy production with thermal analysis under Soret and Dufour effects in MHD flow between convergent and divergent channels, ACS Omega 8 (10) (2023) 9121–9136.
[51] S. Rehman, Hashim, S. Alqahtani, S. Alshehery, Modeling a non-Newtonian nanofluid flow between intersecting planes with slip mechanism, Contin. Mech. Thermodyn. 35 (1) (2023) 61–80.
[52] Z. Asghar, R.S. Saif, A.Z. Ghaffari, Numerical study of boundary stresses on Jeffery-Hamel flow subject to Soret/Dufour effects, Proc. Inst. Mech. Eng. Part C: J. Mech. Eng. Sci. 237 (5) (2023) 1088–1105.
[53] S.M. Garimella, M. Anand, K.R. Rajagopal, Jeffery–Hamel flow of a shear-thinning fluid that mimics the response of viscoplastic materials, Int. J. Non-Linear Mech. 144 (2022) 104084.
[54] T. Hayat, S.A. Khan, S. Momani, Finite difference analysis for entropy optimized flow of Casson fluid with thermo diffusion and diffusion-thermo effects, Int. J. Hydrog. Energy 47 (12) (2022) 8048–8059.
[55] U. Khan, N. Ahmed, S.T. Mohyud-Din, Thermo-diffusion, diffusion-thermo and chemical reaction effects on MHD flow of viscous fluid in divergent and convergent channels, Chem. Eng. Sci. 141 (2016) 17–27.
[56] A.-S.J.A. Al-Saif, A.M. Jasim, New analytical study of the effects thermo-diffusion, diffusion-thermo and chemical reaction of viscous fluid on magneto hydrodynamics flow in divergent and convergent channels, Appl. Math. 10 (4) (2019) 268–300.